2023-07-18

Radar Processing Techniques for Using the LimeSDR Mini as a Short-Range LFM Radar

Jacob Scott Stratford
Brigham Young University

Radar Processing Techniques for Using the LimeSDR

Mini as a Short-Range LFM Radar

Jacob Scott Stratford

A thesis submitted to the faculty of
Brigham Young University
in partial fulfillment of the requirements for the degree of

Masters of Science

David Long, Chair
Willie Harrison
Karl Warnick

Department of Electrical and Computer Engineering

Brigham Young University

Radar Processing Techniques for Using the LimeSDR Mini as a Short-Range LFM Radar

Jacob Scott Stratford
Department of Electrical and Computer Engineering
Masters of Science

BYU Engineering

Abstract

Drone-mounted ground penetrating radar (GPR) has the capability to investigate terrain that is inaccessible or hazardous to humans. A linear frequency-modulated (LFM) radar with the potential for GPR applications is described based on the LimeSDR Mini software defined radio (SDR). Challenges of the LimeSDR Mini radar include the SDR's lack of support for transmitter-receiver synchronization and high bleedthrough leakage. These issues are overcome through corrective software processing techniques including deconvolution of the SDR's system impulse response and digital feed-through nulling. Feed-through nulling is effective at reducing bleedthrough leakage, achieving a 26 dB reduction in power. Although high noise can confound the identification of targets with small radar cross sections in dynamic environments, the LimeSDR Mini radar is demonstrated to display a moving target across multiple ranges. This research demonstrates the increasing accessibility of SDR radar for drone applications, as the LimeSDR Mini is lightweight and low-cost compared to high-end SDRs typically used in SDR radar.

Keywords: feed-through null, ground penetrating radar (GPR), LimeSDR Mini, radar, software defined radio (SDR)

Acknowledgments

I would like to thank Dr. Long for the support and guidance he has provided to me over the last four years. His impact on my education has extended well beyond engineering. I would also like to thank my great GPR team members Hannah Eddy, Levi Powell, and Tayler Livingston for their dedicated work. I also want to thank Nick Kohls and acknowledge his excellent work with the Lime radar before I arrived to the project. A special thanks goes to my parents who encouraged me at every turn. Most of all, thank you to my incredible wife Shea for assisting me with this thesis and with everything else in my life. Your support has kept me going.

Table of Contents

List of Figures

List of Tables

Introduction 1

1.1 Introduction

Drone-mounted ground penetrating radars (GPR)s are a young and challenging technology. In order to penetrate through solid ground and ice, a radar must use long wavelengths. The longer the wavelength, the more effectively it penetrates the Earth. Large wavelengths require large antennas, and large antennas contribute to the weight and drag experienced by a drone.

GPRs also require high bandwidth. The higher the bandwidth of a radar, the better the range resolution. Wide-band antennas are required to obtain high bandwidth while operating at low frequencies, but wide-band antennas also tend to have worse isolation. Poor isolation causes high leakage between antennas, which can drown out weak signals, including the desirable signals that have reflected from tens of meters underground.

These are some of the challenges that must be overcome in designing a drone GPR. Software defined radios (SDR)s are a powerful tool which can aid in the design process for radar applications. SDRs are variable radios which perform a large portion of their processing digitally, rather than in hardware. They support easy software-based reconfiguration that can be applied quickly on an as-needed basis. In some cases, SDRs are employed as the primary radios for standalone radar systems. This thesis explores radar processing techniques for a radar based on the LimeSDR Mini software defined radio, a low-cost SDR with a small form factor which makes it appealing for use in drone GPR applications.

1.2 Background

One significant appeal of drone GPR is that it has the capability to investigate terrain that is dangerous to humans. A major motivator in the research presented in this thesis is the potential for the LimeSDR Mini drone GPR to study inaccessible areas of glaciers, including areas with fissures and otherwise unstable or hazardous terrain. Areas like these present risk to human safety but can be easily navigated using a remotely operated drone GPR.

Before the drone GPR is ready for testing on glaciers, it must successfully demonstrate above-ground radar capabilities. These include the ability to detect reflective targets at different ranges and the ability

to filter out undesirable radar signals such as direct TX-RX leakage, which is often referred to as bleedthrough signal. The radar must also demonstrate consistency between measurements.

Software defined radios provide a good platform for radio systems development, including radars. SDRs are more adaptable than traditional radios, able to function in different configurations with relatively easy operation. For example, the LimeSDR Mini (herein referred to as the Lime) allows a user to change the frequency, bandwidth, sampling rate, and gain of the radio in software through an application programming interface (API) called the SoapySDR library. This flexibility is helpful during radar system development, when many possible design decisions must be compared and evaluated.

In 2021, the LimeSDR Mini was selected for the design of a low-cost drone GPR after being compared with other off-the-shelf SDRs. It was selected primarily because of its low cost and small form factor compared to competing products[1]. This thesis builds on and further develops that radar.

[1] Kohls, "Software Defined Radio Short Range Radar," 2021.

1.3 Thesis Statement and Results Summary

This thesis provides an introduction to radar processing and explores various approaches for minimizing interference and noise to improve target detectability. It develops a radar system compatible with the LimeSDR Mini and discusses the strengths and challenges for such a radar. Shortcomings of the LimeSDR Mini are discussed, including asynchronization issues between the transmitting (TX) and receiving (RX) ports of the SDR. Radar processing compatible with the LimeSDR Mini is discussed and demonstrated in measuring lengths of cable. In conjunction with these, methods for bleedthrough signal reduction are compared and tested, including analog and digital feed-through nulling techniques.

The radar is tested with custom strip-dipole antennas, which are used to test the radar's ability to detect targets at various distances. Although high noise can confound the identification of targets with small radar cross sections in dynamic environments, the LimeSDR Mini radar is demonstrated to display a moving target across multiple ranges. This research demonstrates the increasing accessibility of SDR radar for drone applications, as the LimeSDR Mini is lightweight and low-cost compared to high-end SDRs typically used in SDR radar.

1.4 Roadmap

Chapter 2 provides an introduction to radar, including early innovations in radar technology with an emphasis on GPR. Basic radar theory is also discussed for linear frequency-modulated (LFM) short-range radar systems. Chapter 3 describes the LimeSDR Mini, including its design specifications and its strengths and weaknesses as a radio system for radar application. Design requirements for the LimeSDR Mini GPR are

also discussed. Chapter 4 discusses antennas developed for the GPR. Chapter 5 discusses various radar processing techniques for reducing interference and noise. These techniques include signal windowing, SDR impulse response correction through deconvolution, and digital and analog feed-through nulling techniques. Radar tests which demonstrate these techniques are also documented. Conclusions are provided and suggestions for future work are discussed in Chapter 6.

Radar Background

<div style="text-align: right; font-size: 2em;">*2*</div>

It is useful to explain radar's history, as well as its basic principles before addressing the system design. This chapter provides a review of the basics of radar.

2.1   The History of Radar

One of the first people to speculate on the possibility of radar was Guglielmo Marconi (1874 – 1937), often considered the father of radio. Marconi was an Italian man with a particular interest in the electrical sciences, having studied from a young age the works of James Clerk Maxwell, Heinrich Hertz, Augusto Righi, and other pioneers of electrical engineering. While he is best known for his wireless telegraph, which earned him a Nobel Prize and which was famously used to transmit "S.O.S." from the Titanic, one of his breakthroughs occurred when he observed electromagnetic waves bouncing off metal in 1899. He theorized an early concept in which a radio signal could be transmitted from a ship at sea, which would reflect off other ships or metal sheets along the shore, allowing remote detection in low visibility situations[2]. What Marconi described is the groundwork of modern radar systems.

It took an industrious German by the name of Christian Hülsmeyer to patent a radio-based ship detector in 1903. A prototype soon followed, wherein a signal was widely broadcast, and reflections were picked up by a rotating dipole antenna. The antenna activated a relay and rang an electric bell, indicating the direction, but not the distance, to a ship[3].

Innovation slowly continued. In 1910, the first patent was filed for a ground penetrating radar. In 1924, the United Kingdom's Air Ministry created the Committee for the Scientific Survey of Air Defense (CSSAD), dedicated to exploring how recent advances in science might be applied to deterring hostile aircraft. CSSAD funded the first radio-wave-based aircraft detection system, which succeeded in identifying an airplane from up to eight miles away[4]. In following years, the system was further developed and implemented in various branches of the British military.

The potential for radar increased greatly in the following years as engineers transitioned away from transmitting pulses and tones and instead transmitted chirps, which greatly improved the range resolution. In 1929, W. Stern successfully measured the depth of a glacier[5] using a chirped radar. Over the next decade, many countries developed their own radar defense systems in relative secrecy, although Great Britain

[2] Elsevier Publishing Co, *The Nobel Prize in Physics 1909- Guglielmo Marconi Biographical*, 1967.

[3] Hülsmeyer, *Christian Hülsmeyer and the Early Days of Radar, a Survey. Part II*, 1904.

[4] Watson Jr, *Radar Origins Worldwide: History of its evolution in 13 nations through World War II*, 2009.

[5] Blindow *et al.*, "Ground Penetrating Radar," 2007.

shared its discoveries with the United States and major commonwealth countries[4].

The United States outfitted a battleship with its first fully operational radio-based detection system in 1939, calling it a "Radio Detection and Ranging" (RaDAR) system. Later that year, Germany would instigate the second world war by invading Poland. World War II brought major advances to radar, including the use of portable radar systems to detect mines. These systems were some of the forerunners to modern GPR.

2.2 Drone GPR

In recent decades, GPR has played a large role in environmental, industrial, and archaeological projects. GPR hardware is typically mounted to a cart or trailer which is pushed by hand or pulled by a vehicle. This allows GPR antennas to sit a few inches above the ground, coupling directly into the earth. GPR requires especially long wavelengths in order to penetrate through soil, sand, and rocks, but larger wavelengths make it difficult to see small targets. The GPR's center frequency is picked by evaluating the trade-offs between deeper penetration, finer resolution, and GPR size and weight.

In recent years, there has been interest in operating GPR on aerial drones. Drone GPR is able to access areas that may be too dangerous for humans, and it does so without disturbing the ground it is measuring. Since drones can be programmed to fly certain routes, they may also collect large amounts of data more consistently, more accurately, and more quickly than human-operated GPR.

The high productivity of drone GPR comes at a cost. While cart-based GPRs may sit a few inches above the ground, drones require greater height. They are also susceptible to shifting altitude depending on the topography and weather conditions. When the GPR is positioned more than a half-wavelength above the surface of the Earth, the transmitter cannot couple directly into the ground, and power is reflected off the surface of the earth and into the antennas. These challenges are being overcome by companies like SPH Engineering[6] and MALÅ GeoDrone[7], which have released products and services for drone GPR bathymetry and land surveys.

One of the most compelling stories of drone GPR occurred in 2018, when a team from SPH Engineering located a Lockheed P-38 Lightning aircraft buried in Greenland's ice sheet. The plane had been part of a 6-plane squadron forced to land on the glacier during a storm near the end of WWII, and although all pilots were rescued, the planes were temporarily abandoned. By the time teams returned to recover the aircraft, they had been completely buried in Greenland's shifting landscape. One aircraft was located and recovered in 1992 after years of searching and digging. In 2018, the SPH Engineering team used drone GPR to locate another aircraft more than 100 m below the surface[89].

It is often easier for GPR to reach deeper into glaciers than into other ground types. Many glaciers, particularly in Greenland, are far away

4 Watson Jr, *Radar Origins Worldwide: History of its evolution in 13 nations through World War II*, 2009.

6 SPH Engineering, *Webinar: Basics of ground penetrating radar (GPR) usage with a drone*, 2023.

7 MALÅ, *Airborne Ground Penetrating Radar System: GeoDrone - Airborne GPR made easy*, 2021.

8 UgCS - SPH Engineering, *Expedition to Locate P-38 "Echo" From Lost Squadron just Returned from Greenland's Ice Cap*, 2023.

9 Jensen, *Glacier Girl: The back story - How it got trapped in the ice, and how it got out*, 2007.

Figure 2.1: A P-38 Lightning aircraft known as "Glacier Girl," which is from the same lost WWII squadron as the plane located by SCP engineering. Glacier Girl was located and recovered in 1992, 26 years before SCP Engineering's demonstration.

from sources of RF interference. In addition, the snow and ice constitute a very consistent medium, making foreign objects stand out. In addition to locating buried aircraft, drone GPR has the capability of measuring the different layers in glacial ice, differentiating between new snow and old multi-year ice due to their different dielectric and conductive properties.

While drone GPR has proven effective, it is still a young, expensive technology. The cost of GPR may come down if innovators are able to configure software defined radios (SDRs) to perform GPR tasks.

2.3   Short-Range Radar Basics

Radar uses reflected electromagnetic signals to determine characteristics about a target. All radars have some basic components in common, although radar applications vary widely. A radar requires a signal source (a radio), as well as a transmitter and a receiver. When the radar employs a transceiver with a single antenna, then we call it a monostatic radar. If the transmitter and receiver are distinct but very close to each other relative to the target, then it is called a pseudo-monostatic radar, and many of the radar mathematics may be approximated as if it were a monostatic system. Alternatively, a bistatic radar has a transmitter and receiver at different locations. In this chapter, the math provided describes a monostatic radar, which is the most common.

A radar transmits an electromagnetic signal, then measures the signal that returns after reflecting off one or more targets. Between the time a signal is transmitted and the time it is received, that signal changes depending on the targets' direction, range, velocity, size, and physical properties. When the reflected signal is measured, it may be analyzed to recover some of this information.

It is useful to work through the example. Suppose a signal $s(t)$ is transmitted at time $t = 0$. If a single, stationary point target is positioned some distance R from the transceiver, then the received signal $r(t)$ is the

attenuated and time-delayed copy of $s(t)$

$$r(t) = \alpha s(t - \tau).\tag{2.1}$$

The attenuation factor α depends on the antenna gain, the target range R, and the size and backscatter properties of the target. The time delay τ is the two-way travel time of the signal, given as

$$\tau = \frac{2R}{c}.\tag{2.2}$$

Here, c is the speed of light. Figure 2.2 shows the path of a signal in a stationary radar-target system.
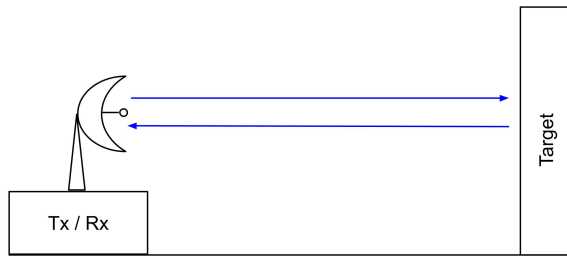
Figure 2.2: A radar transmits a signal, which bounces off a target and returns back to the transceiver.

This thesis discusses the design of a linear frequency modulated (LFM) radar. An LFM radar transmits a chirped signal which increases in frequency with time. An LFM chirp is shown in Figure 2.3, along with its time-delayed echo.

The instantaneous frequency of the transmitted and received signals are $f_t(t)$ and $f_r(t)$, respectively. If an LFM chirp spans τ_c seconds and sweeps from a frequency f_0 up to f_1, then the chirp has bandwidth B and slope S, given by

$$B = f_1 - f_0\tag{2.3}$$

$$S = \frac{B}{\tau_c}.\tag{2.4}$$

An LFM chirp can be described as follows:

$$s(t) = \cos\left(2\pi\left[f_0 t + \frac{S}{2}t^2\right]\right)$$
$$0 \leq t \leq \tau_c.\tag{2.5}$$

If there are multiple targets, then the return signal $r(t)$ is the sum of the return signals reflecting off each of them. If the targets are located at n different distances, this results in n intermediate frequencies f_{IF1}, f_{IF2}... f_{IFn}, as can be seen in Figure 2.4.
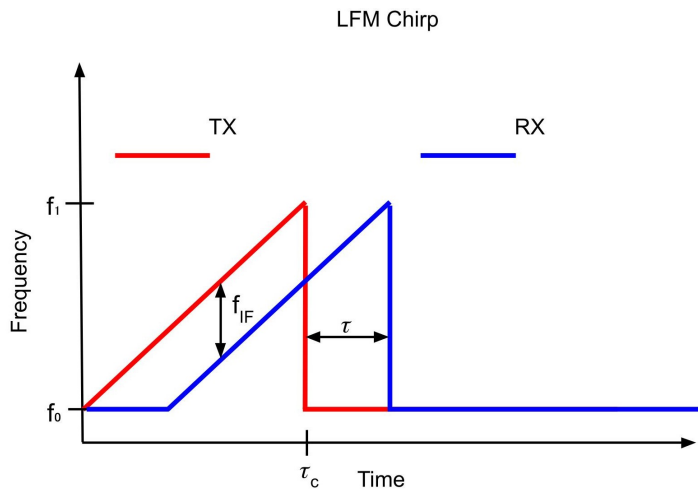
Figure 2.3: An LFM chirp increases linearly in frequency with time.
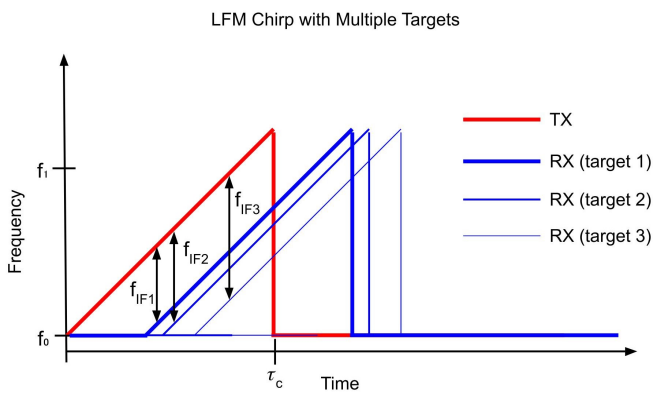
Figure 2.4: When multiple targets are present, the return signal is the sum of the return signal caused by all reflections. This results in multiple intermediate frequencies f_{IF1}... f_{IFn}. Thinner lines represent the decreased return power resulting from greater distance to a target.

In many applications, including the radar presented in this thesis, the transmit signal $s(t)$ is amplitude-modulated to some higher carrier frequency f_c. This is accomplished by mixing the transmit signal with the carrier signal $\cos(2\pi f_c t)$. The mixed signal is obtained by multiplying the two signals in the time domain. Likewise, the received signal is mixed down to or near baseband and lowpass filtered before being sampled. The diagram for a simple SDR-based radar system is shown in Figure 2.5.
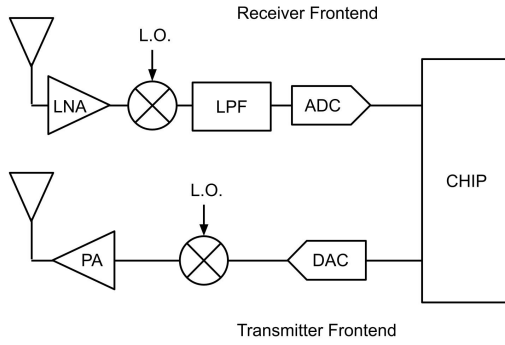
Figure 2.5: A simplified SDR frontend used for LFM radar. The SDR chip produces a digital signal to transmit, which passes through a digital-to-analog converter (DAC), is mixed with the carrier frequency signal produced by a local oscillator (L.O.), and is power amplified (PA) before radiating out of an antenna. Another antenna picks up the received signal which passes through a low-noise amplifier (LNA), is demodulated, is lowpass filtered (LPF), and is passed through an analog-to-digital converter (ADC) before being read into the chip.

Thus, the return signal $r_{\text{demod}}(t)$ fed into the low-pass filter is

$$r_{\text{demod}}(t) = \cos\left(2\pi f_c t\right) \cos\left(2\pi f_c t\right) \alpha \cos\left(2\pi \left[f_0\{t - \tau\} + \frac{S}{2}\{t - \tau\}^2\right]\right),$$

(2.6)

which can be expanded using basic trigonometric identities as

$$r_{\text{demod}}(t) = \frac{1}{2}\alpha\left(\cos\left[2\pi\{f_c + f_c\}t\right] + \cos\left[2\pi\{f_c - f_c\}t\right]\right)$$

$$\cos\left(2\pi\left[f_0\{t - \tau\} + \frac{S}{2}\{t - \tau\}^2\right]\right). \quad (2.7)$$

The lowpass filter removes the $\cos(2\pi\left[f_c + f_c\right]t)$ term and leaves the input to the ADC $r_{\text{LPF}}(t)$, given by

$$r_{\text{LPF}}(t) = \frac{1}{2}\cos\left(2\pi\left[f_c - f_c\right]t\right)\alpha\cos\left(2\pi\left[f_0\{t - \tau\} + \frac{S}{2}\{t - \tau\}^2\right]\right) \quad (2.8)$$

$$= \frac{1}{2}\alpha\cos\left(2\pi\left[f_0\{t - \tau\} + \frac{S}{2}\{t - \tau\}^2\right] + \phi\right), \quad (2.9)$$

which is an attenuated and time-delayed version of the original signal $s(t)$. Due to the unknown phase of the local oscillator during this process, the output has an additional phase offset ϕ.

For short-range radar, the transmitted signal and the received signal overlap in time. The intermediate frequency f_{IF} is the difference between the transmitted signal's instantaneous frequency $f_t(t)$ and the received signal's instantaneous frequency $f_r(t)$, during the time of their overlap. The intermediate frequency depends on the travel time of the signal and on the slope of the chirp, and is given by

$$f_{IF} = f_t(t) - f_r(t) \tag{2.10}$$

$$= \tau S, \tag{2.11}$$

$$\tau \le t \le \tau_c. \tag{2.12}$$

By rearranging, we can find the signal's time of flight, which can in turn be used to find the range to the target

$$\tau = \frac{f_{IF}}{S} \tag{2.13}$$

$$R = \frac{\tau c}{2}. \tag{2.14}$$

Next, we define a time-domain signal $f_{IF}(t)$ called the de-chirped signal by mixing the transmit and receive signals. This can be demonstrated using the complex transmit signal

$$s(t) = \exp\left\{ j2\pi f_0 t + j2\pi \frac{S}{2} t^2 \right\} \tag{2.15}$$

and the complex receive signal in a single-target system

$$r(t) = \alpha \exp\left\{ j2\pi f_0 (t - \tau) + j2\pi \frac{S}{2} (t - \tau)^2 \right\}. \tag{2.16}$$

We mix these signals by multiplying $s(t)$ by the conjugate of $r(t)$ in the time domain and obtain the de-chirped signal

$$f_{IF}(t) = s(t) r(t)^* \tag{2.17}$$

$$= \exp\left(j2\pi \left[f_0 t + \frac{S}{2} t^2 \right] \right) \exp\left(-j2\pi \left[f_0 \{t - \tau\} + \frac{S}{2} \{t - \tau\}^2 \right] \right) \tag{2.18}$$

$$= \exp\left(j2\pi \left[\frac{S}{2} t^2 + f_0 t - \frac{S}{2} \{t - \tau\}^2 - f_0 \{t - \tau\} \right] \right) \tag{2.19}$$

$$= \exp\left(j2\pi \left[\frac{S}{2} t^2 + f_0 t - \frac{S}{2} \{t^2 - 2\tau t + \tau^2\} - f_0 t + f_0 \tau \right] \right) \tag{2.20}$$

$$= \exp\left(j2\pi \left[S\tau t - \frac{S}{2} \tau^2 + f_0 \tau \right] \right) \tag{2.21}$$

$$= \exp(j2\pi S\tau t) \exp\left(j2\pi \left[f_0 \tau - \frac{S}{2} \tau^2 \right] \right) \tag{2.22}$$

$$= \exp(j2\pi S\tau t + \phi), \tag{2.23}$$

10 Easton Jr, *Fourier Methods in Imaging*, 2010.

where ϕ is the phase offset $j2\pi(f_0\tau - \frac{S}{2}\tau^2)$.[10] The de-chirped signal is given over $\tau \leq t \leq \tau_c$, since one or both of the mixer's input signals are zero elsewhere.

An SDR like the LimeSDR Mini takes a receive signal and produces IQ data by mixing the received signal with two carrier signals which are 90 degrees out of phase with each other, then by sampling the two resulting signals. The I and Q data may be interpreted as the real and imaginary portions of a complex receive signal, respectively. Figure 2.6 shows how discrete I and Q samples are typically extracted from a continuous signal r(t)[11].

11 BniLam *et al.*, "Low Cost AoA Unit for IoT Applications," 2019.
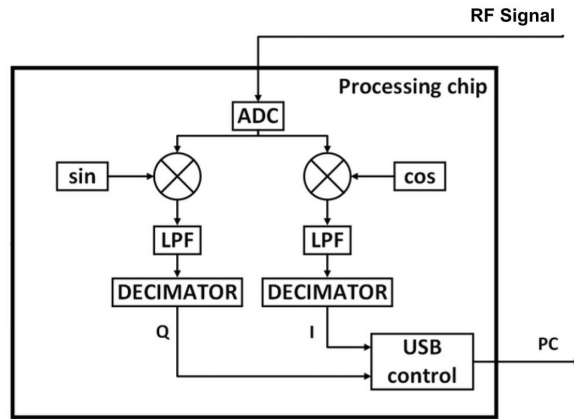
Figure 2.6: Diagram displaying how I and Q data are extracted from an RF signal. The RF signal is split and mixed with some carrier frequency at a 90 degree phase offset, represented by sin and cos.

By summing $(I + jQ)$ at each sample, we produce the discrete complex return signal $r[n]$, where

$$r[n] = I[n] + jQ[n] \tag{2.24}$$

$$= \exp\left(j2\pi\left[f_0\{Tn - \tau\} + \frac{S}{2}\{Tn - \tau\}^2 + \phi\right]\right), \tag{2.25}$$

where the SDR uses a sample frequency of f_s, and T is the sample period $\frac{1}{f_s}$. We likewise define our discrete transmit signal $s[n]$ as

$$s[n] = \exp\left(j2\pi\left[f_0Tn + \frac{S}{2}\{Tn\}^2 + \phi\right]\right). \tag{2.26}$$

$s[n]$ may be interpreted as the samples which are sent to the SDR chip for transmission.

By mixing the discrete signals $s[n]$ and $r[n]$, we get the discrete

de-chirped signal

$$f_{IF}[n] = s[n]r[n]^* \tag{2.27}$$

$$= f_{IF}(Tn) \tag{2.28}$$

$$= \begin{cases} \exp(j2\pi S\tau[Tn] + \phi) & \text{for } \tau \le Tn \le \tau_c \\ 0 & \text{else} \end{cases} \tag{2.29}$$

The intermediate frequency f_{IF} ought to be easily found using the Discrete Fourier transform (DFT). If we take the DFT of the signal $f_{IF}[n]$ over the correct time interval, then f_{IF} falls within the frequency bin corresponding to the DFT's peak.

The range resolution of the radar is directly related to the width of the frequency bins. The DFT can be used to produce an arbitrary number of frequency bins, but if you produce more frequency bins than you have time-domain samples, then the frequency domain data represents an interpolation, and carries no additional information. Let us assume that we take the N-point DFT of N samples of the mixed signal $f_{IF}[n]$, where N is the number of samples in the chirp, f_s is the sample rate, and

$$N = \tau_c f_s. \tag{2.30}$$

Then the frequency bin width is

$$\Delta f = \frac{f_s}{N}. \tag{2.31}$$

The frequency bin width can be used to find the travel time-delay resolution of the radar, which can be used to find the range resolution of the radar. The range resolution can also be thought of as the range at which the two-way travel time Tau equals the sample period of the radio. Range resolution is given by

$$\Delta R = \frac{\Delta f \, c}{2S} = \frac{c}{2f_s}, \tag{2.32}$$

where the ½ factor comes from the two-way travel path of the signal.

It is desirable to have a range-resolution which is as small possible. The range resolution is minimized when the LFM chirp has the highest possible bandwidth. To avoid aliasing, the bandwidth must not exceed the Nyquist rate, which is equal to the sample rate when samples include I and Q data.

Radar with the LimeSDR Mini

<div align="right">

3

</div>

Software defined radios allow a user to change the radio's gain, carrier frequency, filtering effects, and other variables by sending commands to a chip which interfaces with a FPGA and RF module, which contain all the hardware necessary for a variety of applications. This streamlines the configuration process, which makes SDRs especially useful during the design process and in radio systems which are not intended for mass production.

Innovation in SDR technology has led to their increased use, including a rapidly growing interest in using them for radars. This can be clearly seen in the number of academic papers published about them in recent years. Figure 3.1 shows the number of academic journal and conference papers, per year, with metadata including the terms radar and software defined radio in the IEEE Explore archive. For reference, the number of total academic papers published per year worldwide has roughly quadrupled over the same time span[12]. SDR-based radars are being developed or implemented for applications such as weather surveillance [13], space object location [14], forward-scatter radar [15], and ground-penetrating radar [16]. Many of these applications use relatively expensive SDRs with customs FPGA programming

The low-cost GPR discussed in this thesis employs a compact software-defined radio called the LimeSDR Mini through its standard FPGA interface. This chapter offers an introduction to the LimeSDR Mini and its capabilities, its performance issues, and ways to overcome those issues.

3.1   The LimeSDR Mini

The LimeSDR Mini is a low-budget software defined radio produced by Lime Microsystems. Like other SDRs, it consists of a digital system pre-programmed to solve a wide variety of problems in radio communications. The LimeSDR Mini may be configured as a variable RF transmitter or receiver, which permits it to serve a wide range of functions with a relatively simple interface and low cost. It was launched through Crowd Supply, a platform that allows hobbyists to fund product development and projects for startup companies. The LimeSDR Mini was discontinued in 2022, although its popularity spurred the development of the more expensive LimeSDR Mini 2, which is still available for purchase.

[12] White, *Science & Engineering Indicators*, 2019.

[13] Prabaswara *et al.*, "GNU Radio based software-defined FMCW radar for weather surveillance application," 2011.

[14] Jędrzejewski *et al.*, "Passive Space Object Observation using LOFAR Radio Telescope and Software-defined Radio Receiver," 2022.

[15] Hristov *et al.*, "Software defined radio for profile reconstruction in forward scatter radar," 2014.

[16] Carey *et al.*, "Software defined radio for stepped-frequency, ground-penetrating radar," 2017.
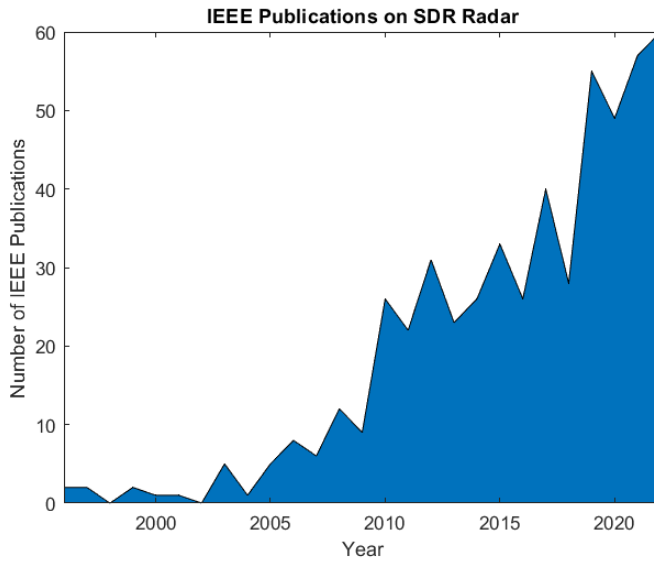
Figure 3.1: Total academic journal and conference papers on SDR radar in the IEEE *Xplore* archive, by year, 1996-2022. The papers included were all those with metadata containing the phrases "Software Defined Radio" and "radar."

The LimeSDR Mini employs the LMS7002M transceiver radio frequency integrated circuit (RFIC), which connects to an Intel Altera Max 10 Field-Programmable Gate Array (FPGA). An analog-to-digital converter (ADC) and digital-to-analog converter (DAC) perform conversion between the continuous-time RF signals and the samples which are stored in a buffer on the FPGA. There are an additional 4 MB of flash memory for data samples, which are sent via USB 3.0 to be stored on a computer, which is necessary for powering and programming the SDR. The SDR's tx and rx frontends each includes a female SMA cable adapter. Its dimensions are 69 mm × 31.4 mm and it weighs 20 grams [17]. The LimeSDR Mini is shown in Figure 3.2.

[17] Lime Microsystems Ltd., *LimeSDR Mini*, 2020.
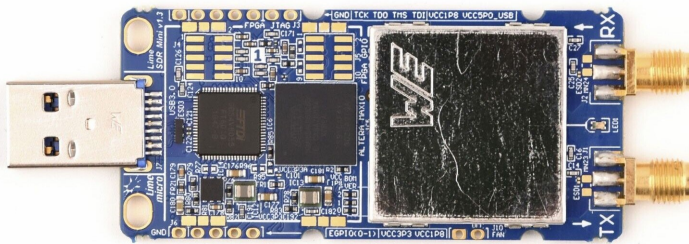
Figure 3.2: The LimeSDR Mini Software Defined Radio. Its compact size and low cost are advantages when used in drone application.

The maximum power output of the LimeSDR Mini is 10 dBm, or 10 mW. The maximum power output is reduced at carrier frequencies above 1.25 GHz [18], though this is much higher than the frequencies used

[18] British Amateur Television Club, *LimeSDR Mini Output Power Levels*, 2019.

for the GPR discussed in this thesis. The transmitter noise figure at maximum gain is 35 dB. The maximum IQ sampling rate supported is 30.72 MSPS.

In 2021, the LimeSDR Mini was selected for the design of a low-cost drone GPR after being compared with other off-the-shelf SDRs (including the USRP B210, a popular high-end SDR). It was selected primarily because of its low cost and small form factor compared to competing products, and because its sampling rate that was sufficiently high for achieving useful range-resolution in a GPR [1]. This thesis builds on and further develops that radar.

[1] Kohls, "Software Defined Radio Short Range Radar," 2021.

3.2   Tx/Rx Synchronization

Unfortunately, the LimeSDR Mini does not support transmitter-receiver synchronization. This introduces a significant challenge in creating a LFM radar, as the radar processing relies on precise and consistent time delays between the transmitted signal and the reflected signal measured at the receiver.

Unfortunately, there is a large discrepancy between the hardware time returned during signal transmission and the hardware time returned during reception. The SoapySDR API permits a user to specify a future time when the SDR transmits or receives or does both. When the chip is instructed to transmit some signal starting at time t and is also instructed to record samples from the receiver beginning at the same time, then the receiver executes the command earlier than the transmitter. The effect is that the received signal appears to be time-delayed by some lag time we may call τ_{FPGA}. The delay time is referred to as τ_{FPGA} because the timing differences are caused in the RF module, the analog and digital converters, and in the FPGA, which handles and stores the samples. This delay exists by design and is hard-coded in the Osmocom GSM (Global System for Mobile Communications) stack.

The delay time τ_{FPGA} varies depending on the SDR configuration. It changes based on the SDR filtering settings, sample rate, and carrier frequency. It is between 2 μs and 80 μs. Once the SDR has been initialized, τ_{FPGA} remains constant until the device is disconnected or reinitialized. When the device is reinitialized multiple times with the same configuration each time, τ_{FPGA} varies from run to run by up to two or three samples.

The hardware delay time τ_{FPGA} can be found by employing the LimeSDR Mini's loopback configuration, where the transmit and receive ports are connected internally, or by connecting the transmit port to the receive port with a very short SMA cable. If an impulse is transmitted, then the received signal is the system impulse response for the transmit-receive configuration. If the chip is instructed to transmit a signal $s[n]$ at time $t > 0$, and the receiver is instructed to store samples $r[n]$ over the same time, then the system impulse response is $h[n]$ such that

$$r[n] = s[n] * h[n]. \tag{3.1}$$

The system impulse response reveals the delay time, as well as any phase changes and filtering that occur during the signal's travel path. Figure 3.3 shows the impulse responses of the LimeSDR Mini after being initialized 10 separate times with the same configuration each time. Only the magnitudes are shown because we are more interested in the delay times than in the specific shapes of the complex impulse responses. The tapering that follows the pulses is also of interest, and represents a slight low-pass filtering effect that is discussed in Chapter 5. For the test that generated these figures, the LimeSDR Mini was configured the same way as it is for most other measurements contained in this thesis. It was set to a carrier frequency of 220 MHz, with a 30 MHz sampling rate.
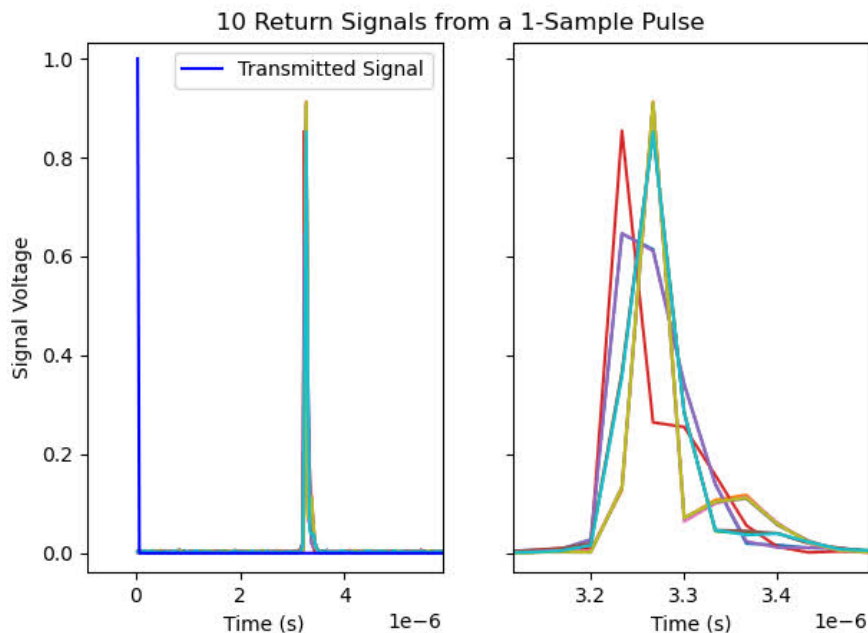
Figure 3.3: The magnitude of the impulse responses of the LimeSDR Mini's transmit-receive system in a loopback configuration. Each of the 10 impulse responses falls into one of 4 recurring IR shapes. Left - impulse responses relative to the transmitted pulse. Right - zoomed image of impulse responses.

If τ_{FPGA} is known, then an LFM radar may determine the range to a target without issue. The delay time calculated in Equation 2.13 is total delay time τ_{IF} where

$$\tau_{IF} = \tau_{\text{target}} + \tau_{\text{FPGA}}, \quad (3.2)$$

and where τ_{target} is the delay time caused by the signal's two-way travel time to the target and back. The target's range can then be found by solving for τ_{target} and adapting equation 2.10 to obtain

$$R = \frac{\tau_{\text{target}} c}{2}. \quad (3.3)$$

3.3   Radar Requirements

The requirements of a drone GPR are straightforward. It must be able to differentiate between different materials occurring at different depths within and below the glacier. These layers may include layers of snow, ice, rocks, and dirt or debris. With radar post-processing, it is generally possible to distinguish these layers if (1) the radar can discriminate between above-ground targets at different ranges, and (2) if the radar is sensitive enough to pick up the return signal despite the extinction loss of the glacier medium. Another requirement is that the GPR must be light enough to be carried by the drone, including the GPR's power source, antennas, and operational computer for storing measurements. Other design considerations depend on the drone, the ground medium, and desired outcomes of the survey.

For this research, the drone assumed is the DJI Matrice 600 Pro, a 9.5 kg, 6–propellered drone measuring 1668 mm × 1518 mm × 727 mm. The drone can carry a maximum payload of 6 kg (13.2 lb) at sea level, with a hovering time of 16 minutes (32 minutes without any payload).[19] Because the GPR will be used on glaciers at altitudes up to 3300 m, low air pressure reduces the drone's payload capacity and hover time. According to the researchers conducting the survey, in order to ensure that the drone can carry the GPR, the entire GPR system must weigh less than or equal to 5 lb. If the GPR weighs less than this, then the drone's battery life is extended, enabling longer and more distant surveys. In addition, the GPR should be as compact as possible to avoid interfering with the airflow below the drone. The GPR must also be as cheap as possible, without compromising performance.

[19] DJI, *Matrice 600 pro user manual*, 2017.

The LimeSDR Mini is both low-cost and lightweight. Since the maximum sample rate is 30.72 MHz, the maximum bandwidth B of the LFM chirp is also 30.72 MHz, and the best range resolution ΔR can be calculated using Equation 2.32 as

$$\Delta R = \frac{c}{2f_s} \tag{3.4}$$

$$= \frac{\left(2.998 \times 10^8 \, \frac{m}{s}\right)}{(2)\left(3.072 \times 10^7 \, \frac{1}{s}\right)} \tag{3.5}$$

$$= 4.880 \text{ m}, \tag{3.6}$$

or roughly 5 m. This is not a particularly good range resolution for a GPR, but glaciers are deep, and there are ice layers of interest sufficiently deep for the data to be meaningful. However, the GPR must be able to capture information about layers several range-bins deep, tens of meters below the surface. For this reason, a carrier frequency of 220 MHz was selected for the radar. The chirp's center frequency of 235 MHz has a wavelength of roughly 1.3 m, which is large enough to penetrate many tens of meters into dry snow. Above this wavelength, the required antenna size becomes a serious issue for the drone.

3.4 Software

The LimeSDR Mini can be operated through the Soapy SDR Library, created by Pothosware. Soapy is an open source generalized API for managing software defined radios. It can be used to configure dozens of different SDR models from several different companies using a wide array of software modules, which contain the particular driver libraries required for each device.

The Soapy SDR Library defines functions that are common to most SDRs. For example, it can be used to set the gains of the transmitter and receiver, set the carrier frequency, and set the sampling rate.

A major benefit to using the Soapy SDR library is that any software written for the LimeSDR Mini can be easily updated to function with other common SDRs. SoapySDR's flexibility, abstraction, and well-managed documentation make it an excellent choice for software development for the LimeSDR Mini GPR.

Antennas of the LimeSDR Radar

4

4.1 Introduction

The purpose of an antenna is to transmit the electrical signals from a radio source into electromagnetic waves propagating in the air, and vice versa. Antennas can achieve this due to their conductivity and their special geometries, which are resonant at certain electromagnetic frequencies. Some of the important metrics for evaluating antennas include frequency, operational bandwidth, gain, and isolation relative to other antennas in transceiver systems.

Antennas employed on a drone GPR must be designed to resonate at the GPR's carrier frequency and across the radar's full bandwidth. In addition, the antennas ideally have high gain and high isolation, concentrating more power into the ground and less toward each other. Radar antennas with low isolation reduce receiver sensitivity and impede detectability of weaker signals.

The LimeSDR Mini requires two antennas – one for transmitting and one for receiving. Recall that we want to maximize the radar bandwidth to achieve the finest range resolution. Since the LimeSDR Mini has a maximum IQ sampling rate of 30 MHz, the bandwidth of the radar's transmitted signal cannot exceed 30 MHz without experiencing aliasing. Thus, the radar antennas require a minimum operational bandwidth of 30 MHz. Antenna bandwidth is defined as the bandwidth over which the antennas S11 parameter is below -10 dB, meaning all frequencies at which the antennas convert at least 90 percent of power from the feed into transmitted electromagnetic waves (and a small amount of resistive heat).

Since the radar uses a carrier frequency of 225 MHz, an operational bandwidth of 30 MHz corresponds to the frequencies spanning 225 MHz–255 MHz. However, the radar system is designed to accommodate different SDRs should the need arise, so it is worthwhile to select antennas with a bandwidth of 60 MHz or more. This allows them to support higher bandwidths should a user wish to employ an SDR with higher sampling rates than those of the LimeSDR Mini. The antennas should also have the highest gains and isolation possible.

Table 4.1: Measurement and performance comparison between strip dipole and dipole antennas.

Measurement	Strip Antenna	Dipole Antenna
Length	526 mm	600 mm
Width	50 mm	N/A
Thickness (diameter)	1.75 mm	3.18 mm
Minimum Isolation	-28.2 dB (230 MHz)	-29.0 dB (225 MHz)
Maximum Isolation	-30.0 (282 MHz)	-33.4 dB (255 MHz)
Weight (lbs)	0.17	0.09
Max Gain	2.13 dB	2.11 dB
Absolute Bandwidth	58 MHz	32 MHz

4.2 Strip Dipole Antennas

The antennas used for radar testing in this thesis are strip dipole antennas designed by Tayler Livingston[20]. The antennas are created by attaching an SMA transmission line feed to two copper sheets as shown in Figure 4.1. Each copper sheet is 260 mm x 50 mm x 1.75 mm, and the sheets in each antenna are separated by 6 mm.

[20] Livingston, "Comparison of Compact Very High Frequency (VHF) Antennas for Small Airborne Ground Penetrating Radar," 2023, not yet published.

Strip Antenna Dimensions

Length = 260 mm

Copper Plate   Feed   Copper Plate   Width = 50 mm

Gap = 6 mm
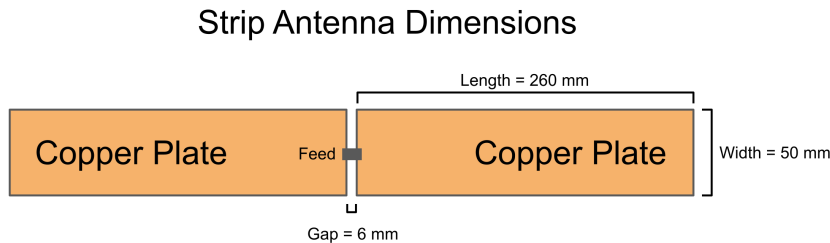
Figure 4.1: Dimensions for the strip antenna used for the LimeSDR Mini radar. The antenna is made of two copper plates with dimensions 260 mm × 50 mm × 1.75 mm which are separated by 6 mm and are connected with a feed to an SMA adapter.

Strip dipole antennas represent a slight deviation from dipole antennas, where conductive plates replace the dipole's conductive wires. The dipole antenna is lightweight, has great isolation, and is easy to construct, however, it also has a narrow operational bandwidth relative to its resonant frequency, making it not ideal for broadband GPR. The strip dipole antenna changes the geometry of the dipole to achieve a wider bandwidth at the cost of isolation.

Some useful performance metrics for the strip antenna are shown in Table 4.1. The metrics for a dipole with the same center frequency are also provided for comparison. The strip dipole antenna meets all the requirements for a drone GPR in the desired frequency range.

Applied Radar Processing Techniques

The previous chapters have introduced the basics of LFM radar, challenges in using the LimeSDR Mini radio for radar, and the antennas used on the Lime radar system. This chapter dives deeper into the signal processing used on the radar, including a method for solving the synchronization problem and multiple techniques capable of reducing bleedthrough power. These signal processing techniques are described and demonstrated with the radar. The most effective ones are used in radar system testing, in which the radar is used to identify a corner reflector moving across various ranges.

5.1 Radar Processing Verification

The short-range radar processing can be tested by comparing the delay time between transmitted and received signals using two methods. The first method is the same as the impulse response test described in Section 3.2. That is, the delay time is found by transmitting a single 1-sample pulse at hardware time $t = 0$, and then by reading the hardware time when the same pulse is observed on the receiver. The second method consists of applying the radar processing described in Chapter 2, where the delay time is found using the intermediate frequency, which is the frequency bin with maximum power in the mixed signal's DFT.

The setup for this test requires placing the SDR in the loopback configuration, where the TX port is connected to the RX port via a short transmission line cable. Then, two distinct signals are transmitted one after the other - first the pulse, then the chirp. Figure 5.1 shows the transmitted signals and received signals.

In this test, most of the transmitted power is seen at the receiver after a 97 sample delay. Since the SDR sample rate is 30 MHz, this equates to a TX-RX delay time of 97 samples$/(30 \times 10^6$ samples per second$) = 3.233$ μs.

Since the sample period is

$$T_s = \frac{1}{f_s} = 33.33 \text{ ns,} \qquad (5.1)$$

we expect the TX-RX delay above to be accurate to within $\pm T_s/2$ or to within 16.67 nanoseconds.

The delay time is then calculated again using the chirp. The transmitted pulse is mixed with the received pulse in the time domain to produce the de-chirped signal $f_{IF}[n]$, shown in Figure 5.2. For a radar-target
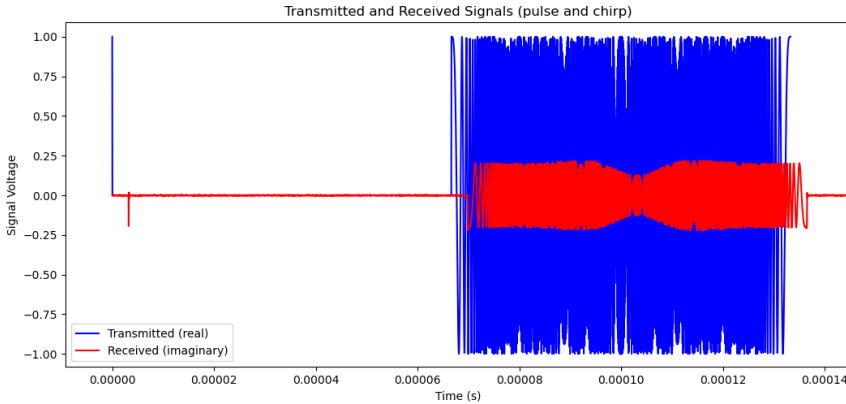
Figure 5.1: Transmitted and received signals in the radar processing verification test. A pulse is transmitted, followed by a chirp. The imaginary part of the received signal is shown because the system impulse response includes a near 90-degree phase change, making the real part of the received pulse very small.

system, we only consider $f_{IF}[n]$ over the bounds given in Equation 2.27. Since the LimeSDR Mini has an inherent TX-RX delay, we must also throw out additional samples. The pulse test gave an estimated delay of 97 samples, so we must throw out at least the samples $n = 0...96$. In this test, the first 105 samples are thrown out. This is to avoid introducing transients in $f_{IF}[n]$ caused by the ringing in the Lime's system impulse response. The imperfect system impulse response also causes the minor filtering responsible for the amplitude dip in the centers of the received chirp and the de-chirped signals.
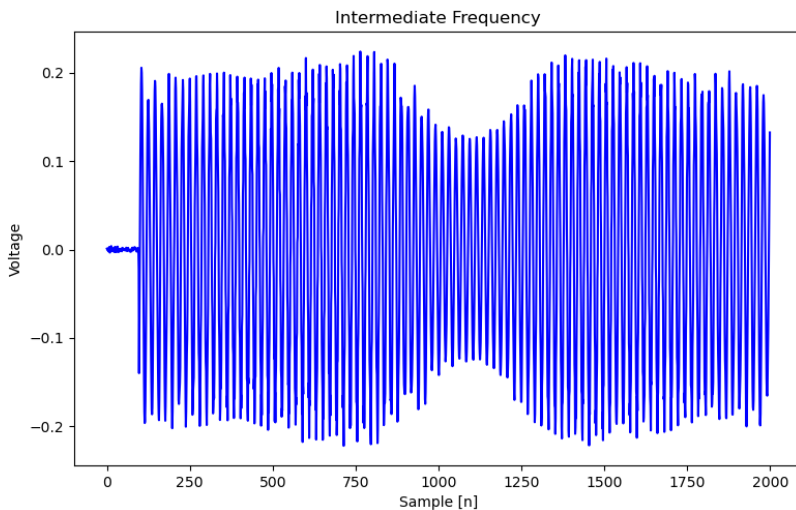
Figure 5.2: De-chirped signal in the radar processing verification test. The dip in the center is a result of slight filtering introduced by the LimeSDR Mini's system impulse response.

The FFT of $f_{IF}[n]$ over the bounds $105 \leq n \leq N - 1$ is shown in

Figure 5.3, where the x-axis has been labeled in frequency bins and time-delay bins, according to relationships given in Equation 2.13 and 2.14.

The LFM radar processing method produces a peak indicating a delay time estimate of 3.235 µs. This is a difference of ~ 2 ns from the pulse sample estimate, well within the 16.67 ns margin for error.
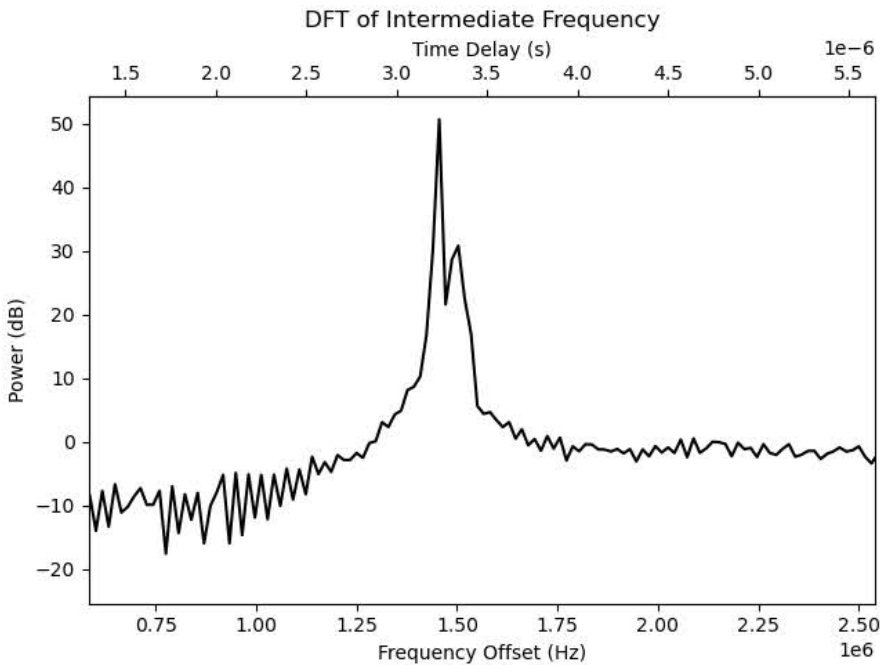
Figure 5.3: FFT of the de-chirped signal. This is also known as range-compressed data.

In the test just described, it was trivial to determine the bounds of n for $f_{IF}[n]$ because an estimate of the TX-RX delay time already existed. Usually the delay time τ is unknown, such as when a target exists at an unknown distance. If τ is unknown, $f_{IF}[n]$ is bounded by $n_1 \leq n \leq n_2$ where n_1 is equal to the largest possible delay (in samples) between the transmitted signal and the returned echo. If earlier samples are included, then the signal might include leading zeros like those seen in Figure 5.2. Note that the leading zeros were removed from the signal before calculating the FFT shown in Figure 5.3. The upper bound n_2 corresponds to the last sample in the transmitted signal. The drawback to removing samples is that the frequency bin size of the FFT increases, as does the range resolution. If $\tau \ll \tau_c$, then this affect is negligible.

5.2 Windowing

The SNR of a de-chirped signal can improve if a window is applied to it, though it can slightly reduce the range resolution. Signal windowing is a method of weighting certain samples in the signal in order to alter the signal's FFT. The most popular windows give greater weight to the samples in the middle of the signal, and less weight to the samples at

the beginning and end of the signal. The effect is that the samples at the beginning and end of the signal have a smaller effect on the FFT. Figure 5.5 shows a windowed and unwindowed signal in the time domain, and 5.4 shows a windowed and unwindowed signal in the frequency domain. These signals are bounded by $n_1 \leq n \leq n_2$, where $n_1 = 100$ and n_2 is the number of transmitted samples. The window in use is the Hamming window.
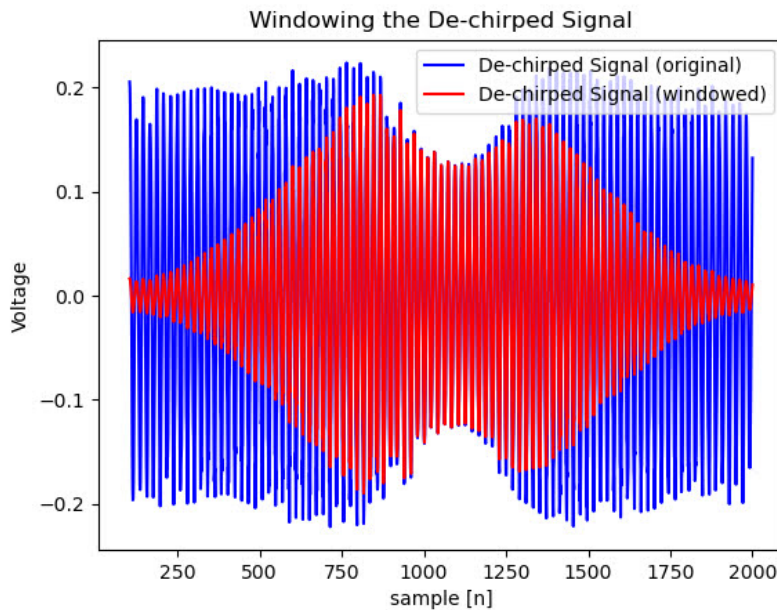
Figure 5.4: A de-chirped signal with and without a window.

There is an intuitive reason for why windowing a signal reduces its FFT sidelobes. In the unwindowed time-domain signal, there is a transient change from last symbol "wrapping around" to the first symbol. Though the frequency is the same at both ends, the phase is not. This is equivalent to a signal being windowed by a rect function, and a time-domain rect function translates to a frequency-domain sinc function. The sidelobes in Figure 5.4 are the manifestation of that sinc function. The window, however, approximates a Gaussian curve in the time domain. A time-domain Gaussian translates to a frequency-domain Gaussian. Since a Gaussian has no sidelobes, the windowed signal's FFT has reduced sidelobes. The cost of this sidelobe reduction is that the main lobe becomes shorter and wider. This represents a decrease in spectral resolution, which can negatively affect range resolution.

The tradeoffs in window selection include frequency resolution (width of the main lobe), amplitude accuracy, and spectral leakage.[21][22] Since the GPR range-compressed data has FFT peaks which are near each other (due to the feed-through signal discussed below), we are particularly interested in windows which have good frequency resolution

21 Harris, "On the use of windows for harmonic analysis with the discrete Fourier transform," 1978.

22 LDS Dactron, *Application Note ANO14 - Understanding FFT Windows*, 2003.
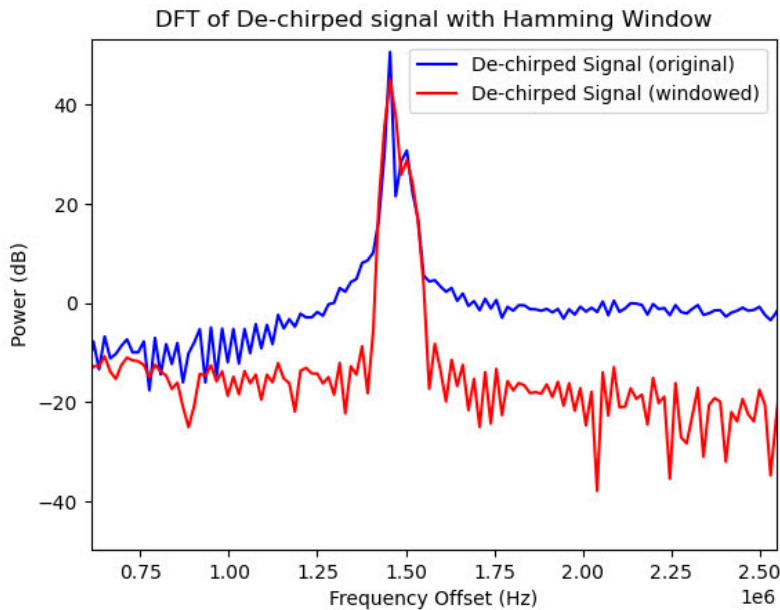
Figure 5.5: The DFT of a de-chirped signal with and without a Hamming window.

Table 5.1: Common windows and their general performance in various metrics.

Window	Frequency Resolution	Amplitude Accuracy	Spectral Leakage	Highest Sidelobe
Barlett	Good	Fair	Fair	-26 dB
Blackman	Poor	Good	Best	-74 dB
Flat top	Poor	Best	Good	-93 dB
Hanning	Good	Fair	Good	-32 dB
Hamming	Good	Fair	Fair	-42 dB
Kaiser-Bessel	Fair	Good	Good	-70 dB
None	Best	Poor	Poor	-13 dB
Tukey	Good	Poor	Poor	-13 dB
Welch	Good	Fair	Good	-21 dB

and low sidelobes near the main lobe. Table 5.1 shows the tradeoffs between the most common window types.

The Hamming window was selected for the radar because its highest side lobes are 42 dB below the main lobe, which is the greatest difference among all the windows with good frequency resolution, meaning narrow main lobes.

5.3   Deconvolution of the SDR Impulse Response

In Chapter 3 we discussed how the LimeSDR Mini has an impulse response $h[n]$, through which the transmitted samples $s[n]$ are filtered before being received and stored in the Lime's receive buffer. When the

Lime is set to a 220 MHz carrier frequency and a 30 MHz sampling rate with default gain, the impulse response includes the hardware delay τ_{FPGA} of about 96 or 97 samples. It also includes an attenuation effect, as well as minor filtering which affects the phase and frequency response of the signal. The time delay shifts the range-compressed data relative to the range bins, and the filtering alters the envelope of the LFM chirp, which can introduce additional noise in the range-compressed data.

Since the system impulse response can be measured, assuming it remains fixed, it can also be removed from the received signal. This can be done through frequency domain deconvolution. The convolution theorem states that the Fourier Transform of two convolved signals is equal to the point-wise product of the Fourier Transforms of each of the signals. In the case of discrete signals, this applies to the Discrete Fourier Transform (DFT) if the discrete signals undergo circular convolution. The DFT of a signal $x[n]$ is defined as

$$X[k] = F\{x\} = \sum_{n=0}^{N-1} x[n]e^{-j\frac{2\pi}{N}nk}, \tag{5.2}$$

and the cyclic convolution theorem for the DFT is

$$(x * y) = XY, \tag{5.3}$$

where X is the DFT of x, and Y is the DFT of y.

The convolution theorem can be used to de-convolve the signals $s[n]$ and $h[n]$ from $r[n]$. Since $r[n]$ does not strictly represent a circular convolution, care must be taken to ensure that both $s[n]$ and $h[n]$ have sufficient zero-padding to produce a linear convolution equivalent to circular convolution. If this criterion is met, then Equation 3.1 may be rewritten as

$$R[k] = S[k]H[k]. \tag{5.4}$$

This relationship describes an idealized, noiseless loopback system.

In real radar applications, we cannot assume that the system is noiseless, nor that there is only one travel path for the signal. If the SDR's internal system has an impulse response $h[n]$, then the exterior system must have its own impulse response, which we call $d[n]$. The impulse response of the exterior system describes reflections from multiple targets, where each point target contributes a time-delayed echo of the transmitted signal.

If Gaussian noise is added to the system, along with an impulse response $h[n]$, then the relationship between the transmitted signal $s[n]$ and the received signal $r[n]$ can be described as

$$r[n] = s[n] * h[n] * d[n] + v_1[n], \tag{5.5}$$

where $v_1[n]$ is uncorrelated Gaussian noise with variance σ_1^2. The goal is to find an estimate for a signal $s[n] * d[n]$, which represents a convolution

of the transmitted signal with the impulse response of the target system. We call this signal $x[n]$:

$$x[n] = s[n] * d[n]. \tag{5.6}$$

To find $x[n]$, we can use our estimate of h[n] which we found by transmitting and receiving a pulse when no targets were present. We call this estimate $\hat{h}[n]$, and define it as

$$\hat{h}[n] = h[n] + v_2[n], \tag{5.7}$$

where $v_2[n]$ is uncorrelated Gaussian noise with variance σ_2^2. In our effort to find $x[n]$, the other tools at our disposal include the known transmit signal $s[n]$, the known received signal $r[n]$, and the convolution theorem.

We combine Equations 5.5 and Equation 5.7 to produce

$$r[n] = s[n] * (\hat{h}[n] - v_2[n]) * d[n] + v_1[n] \tag{5.8}$$

$$= s[n] * \hat{h}[n] * d[n] - s[n] * v_2[n] * d[n] + v_1[n]. \tag{5.9}$$

Next, we convert both sides of the equation to the frequency domain using the DFT

$$R[k] = S[k]\hat{H}[k]D[k] - S[k]V_2[k]D[k] + V_1[k]. \tag{5.10}$$

Then we rearrange and substitute to solve for $X[k]$

$$S[k] * D[k] = \frac{R[k] - V_1[k]}{\hat{H}[k] - V_2[k]} \tag{5.11}$$

$$X[k] = \frac{R[k] - V_1[k]}{\hat{H}[k] - V_2[k]}. \tag{5.12}$$

A conditional expectation estimator for $X[k]$ can then be calculated as

$$\hat{X}[k] = E\left\{X[k]|R[k], \hat{H}[k]\right\}. \tag{5.13}$$

Since $R[k]$ and $\hat{H}[k]$ are known and $v_1[k]$ and $v_2[k]$ are independent, we can simplify to get

$$\hat{X}[k] = E\left\{X[k]|R[k], \hat{H}[k]\right\} \tag{5.14}$$

$$= E\left\{\frac{R[k] - V_1[k]}{\hat{H}[k] - V_2[k]}|R[k], \hat{H}[k]\right\} \tag{5.15}$$

$$= \frac{E\left\{R[k] - V_1[k]|R[k], \hat{H}[k]\right\}}{E\left\{\hat{H}[k] - V_2[k]|R[k], \hat{H}[k]\right\}} \tag{5.16}$$

$$= \frac{R[k] - E\left\{V_1[k]|R[k], \hat{H}[k]\right\}}{\hat{H}[k] - E\left\{V_2[k]|R[k], \hat{H}[k]\right\}} \tag{5.17}$$

$$= \frac{R[k] - E\left\{V_1[k]\right\}}{\hat{H}[k] - E\left\{V_2[k]\right\}}. \tag{5.18}$$

$v_1[n]$ and $v_2[n]$ are Gaussian, and the distribution for any sample of the DFT of a Gaussian signal with variance σ^2 is given by

$$X[k] \sim N\left(0, \frac{\sigma^2}{2N}\right), \tag{5.19}$$

$$x \sim N\left(0, \sigma^2\right). \tag{5.20}$$

Thus, all samples of the DFT of the $v_1[n]$ and $v_2[n]$ have an expected value of 0, and

$$\hat{X}[k] = E\left\{X[k]|R[k], \hat{H}[k]\right\} \tag{5.21}$$

$$= \frac{R[k]}{\hat{H}[k]} \tag{5.22}$$

The time-domain estimate of $x[n]$ is then $\hat{x}[n]$, equal to the inverse DFT

$$\hat{x}[n] = F^{-1}\left\{\frac{R[k]}{\hat{H}[k]}\right\} \tag{5.23}$$

$R[k]$ and $\hat{H}[k]$ can be found using the fast Fourier Transform (FFT), an efficient algorithm for calculating the DFT. The DFTs of $\hat{h}[n]$ and $r[n]$ can be written a

$$\hat{H}[k] = \sum_{n=0}^{N-1} \hat{h}[n]e^{-j\frac{2\pi}{N}kn} \tag{5.24}$$

and

$$R[k] = \sum_{n=0}^{N-1} r[n]e^{-j\frac{2\pi}{N}kn}. \tag{5.25}$$

All that remains is to choose the bounds over which $r[n]$ and $\hat{h}[n]$ are be defined to ensure that linear convolution between them produces the same result as circular convolution. $r[n]$ contains nonzero samples spanning from n_1 to n_2, where $n_1 = \tau_{\text{FPGA}}/T$ and $n_2 = (\tau_{\text{FPGA}} + \tau_{\text{target}} + \tau_c)/T$. τ_{target} represents the longest travel path to and return from a target. $r[n]$ must be defined for at least $n_2 + n_3$ samples, where $h[n3 - 1]$ is the last non-zero sample in the impulse response estimate. A safe approach is to define $r[n]$ over $0 \le n \le 2N - 1$, where N is the number of samples in the transmitted chirp. An example of a received impulse response $h[n]$ is shown in Figure 5.6. Any samples not associated with the impulse have been manually set to zero, to minimize noise.

The 2N-point FFT is taken of r[n] and of h[n], and are shown in Figure 5.7, along with $\hat{x}[n]$, which is produced by taking the inverse FFT (IFFT) of the elementwise quotient $R[k]/\hat{H}[k]$. Figure 5.8 shows a comparison between $r[n]$ and $s[n]$ and between the $x[n]$ and $s[n]$. $x[n]$ much more closely matches the original signal $s[n]$. The trailing zeros in $x[n]$ exist because it is produced by taking the inverse FFT of a length-$2N$ signal and must also have $2N$ samples.
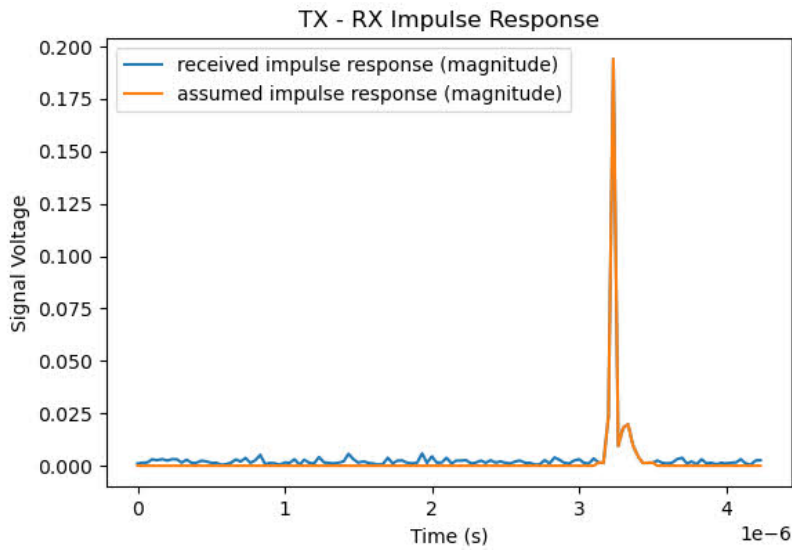
Figure 5.6: The measured impulse response of the LimeSDR Mini. Non-critical samples were manually set to zero to reduce noise.
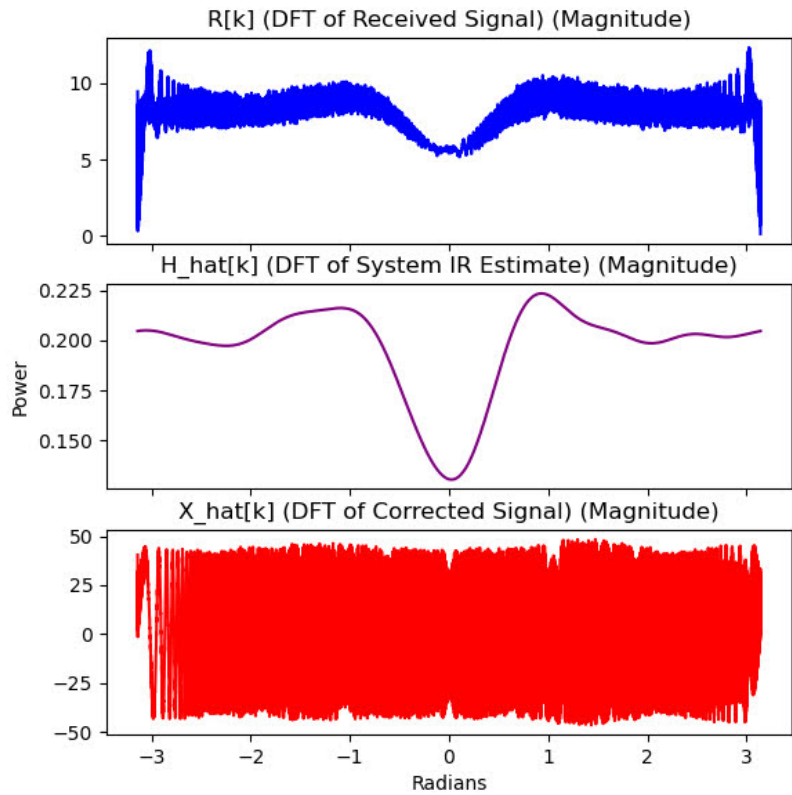

Figure 5.7: The DFTs of $r[k]$, $\hat{x}[n]$, and $\hat{h}[k]$. $\hat{x}[n]$ is produced by dividing the DFT of $r[k]$ by the DFT of $\hat{h}[k]$.
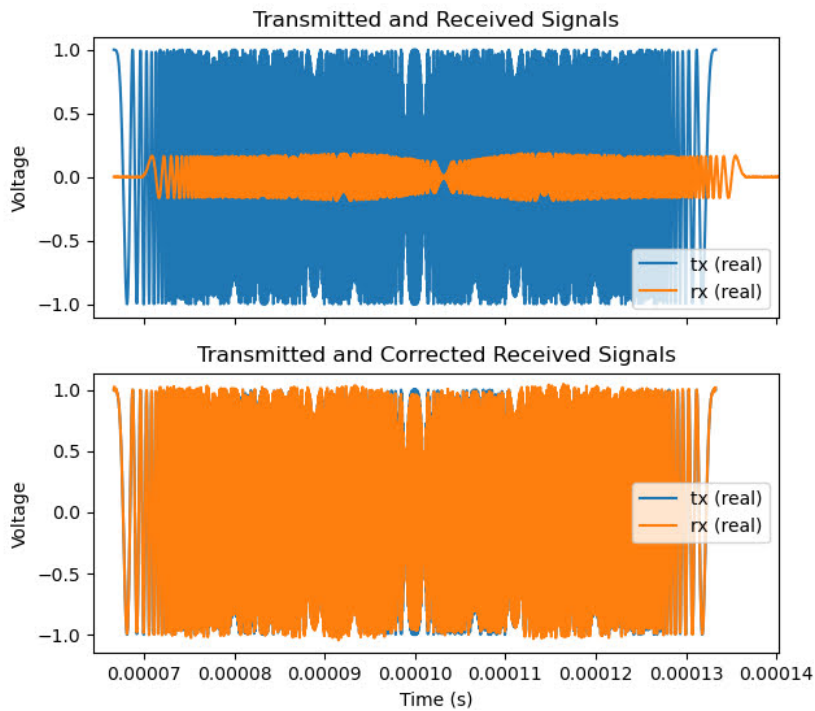
Figure 5.8: Transmitted and received signals before and after applying deconvolution correction.

Since the radar is in a loopback configuration, the FFT of the de-chirped corrected signal includes a large spike at the zero frequency bin (DC). This is because the only time delay present in the received signal is τ_{FPGA}, which is removed during deconvolution. Figure 5.9 shows the FFT of the de-chirped corrected signal, including the DC spike.

The benefit to correcting a signal through deconvolution is that it removes undesired filtering affects from the received signal. To produce range-compressed data, the received signal is mixed with the transmitted signal under the assumption that the received signal is a clean LFM chirp. By digitally correcting the SDR's impulse response, we make the received signal more closely resemble a time-delayed copy (or copies) of the transmitted LFM chirp.

When the SDR is mounted on a drone with antennas with imperfect isolation, the system impulse response $h[n]$ is different than the one shown here. It is includes reflections off the drone, as well as a signal traveling directly from the transmitting antenna to the receiving antenna. Signal correction via deconvolution reduces those effects, especially when combined with feed-through nulling techniques described in Section 5.4.

Deconvolution correction can be be applied as follows. First, the system impulse response $h[n]$ is estimated by transmitting a pulse with
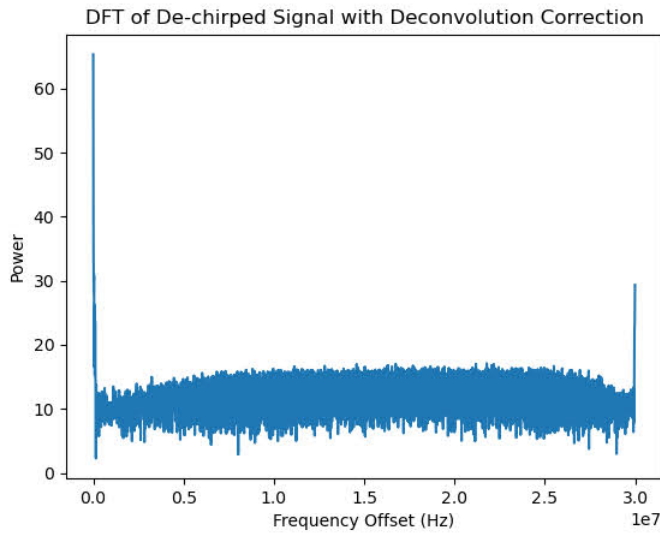
Figure 5.9: The DFT of a the de-chirped signal created by mixing the transmitted signal $s[n]$ with the conjugate of the corrected receive signal $\hat{x}^*[n]$. Deconvolution correction removes any return signal time delays that are not caused by a target, causing the frequency offset to register high power at zero.

no target present. If the GPR is on a drone, then this can be done by flying the drone to some height at which any reflections off the ground do not affect the estimate. For example, if $\hat{h}[n]$ is defined extending 10 samples past the main pulse, and the range resolution is 5 m, then the drone must be at least $10 \cdot 5 = 50$ m above the surface. Then, the drone is lowered back down and transmits LFM chirps and stores the received samples as normal. Later, the received signal is deconvolved from the impulse response as outlined in this section, before being de-chirped and transformed to the frequency domain.

5.4 Bleedthrough Signal and Feed-through Nulling

When a radar system has separate transmit and receive antennas, some of the transmitted signal travels directly from the transmitter into the receiver. This is called the bleedthrough signal, and it is an undesirable effect. In this section, the portion of the received signal that is a result of the transmitted signal reflecting off targets is referred to as the return signal or the target return signal. The signal observed at the receiver is the sum of the bleedthrough signal, the return signal, and noise. This section discusses the bleedthrough signal and ways to reduce its negative effects.

5.4.1 Bleedthrough Signal

Since the travel path of the bleedthrough signal is much shorter than the travel path of the return signal, it is common for the bleedthrough signal to be significantly more powerful than the return signal. If the

bleedthrough signal is large enough, it can reduce the sensitivity of the receiver, which has a limited dynamic range. Worse, the sidelobes of the bleedthrough signal can overwhelm peaks from the return signal in range-compressed data, particularly if the targets are close-range. Figure 5.10 shows the travel paths of the bleedthrough signal and the return signal in a single-target system.
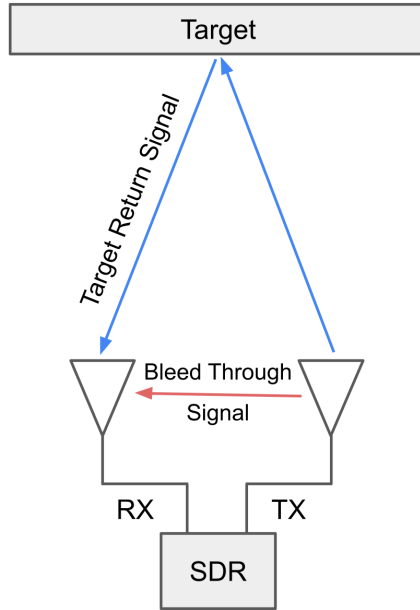
Figure 5.10:   The bleedthrough signal includes any signal which leaks from the transmitter directly into the receiver, without reflecting off a target.

The delay time of the bleedthrough signal equals the SDR delay time τ_{FPGA} plus the travel time of the signal, including travel time through transmission cables and through the air between the antennas. If the travel time is less than the radar time resolution $\Delta\tau$, then the delay time is approximately equal to τ_{FPGA}.

In the range-compressed data, if a target's range bin is too close to the bleedthrough range bin, then it maybe overwhelmed by the spectral leakage of the bleedthrough signal. If the target is too far away, then the return power drops off exponentially, eventually falling below the noise floor.

The power of the bleedthrough signal can be calculated using the Friis Transmissiion Formula, which relates the power received at an antenna to the transmitted power from another antenna when the antennas have direct line of sight. The Friis transmission forumla is given by

$$\frac{P_r^{BT}}{P_t} = \left(\frac{\lambda}{2\pi d}\right)^2 G_t G_r, \tag{5.26}$$

where P_r^{BT} is the bleedthrough power in the received signal, P_t is the

power in the transmitted signal, λ is the wavelength, d is the distance between transmitter and receiver, and G_t and G_r are the gains of the transmit and receive antennas in the directions which point toward each other. Another way to consider this relationship is that the right side of the equation is equal to the antenna isolation.

The power in the return signal which has reflected off a target can be calculated using the radar equation, given by

$$\frac{P_r^R}{P_t} = \frac{\lambda^2 G_t G_r}{(4\pi)^3 R^4} \sigma,$$
(5.27)

where P_r^R is the power in the received signal which has reflected off a target, G_t is the gain of the transmit antenna, and G_r is the gain of the receive antenna, each in the direction of the target. σ is the radar cross section, which describes how large and reflective the target appears to the signal and has units m^2.

The simplest way to decrease the bleedthrough signal relative to the return signal is by placing the antennas farther apart, thereby increasing d without increasing R. If d is doubled, then P_r^R is reduced by 6 dB. It is difficult to mount antennas far apart when the radar system must be contained on a small drone. The bleedthrough signal can also be reduced by increasing the isolation between antennas. For example, antennas may be designed to have broadside nulls in the antenna pattern, where the antennas face each other. This also can be difficult for drone GPRs, which tend to require broadband antennas which have worse isolation than alternative antennas such as the dipole. The strip antennas discussed in Chapter 4 were chosen for use with the radar because they have relatively high isolation while meeting broadband requirements.

The bleedthrough power and the return power are estimated for the drone GPR at different ranges and are plotted in Figure 5.11. This assumes an antenna separation d of 0.7 m, and average antenna gains of 2.13 dB (1.63) in the direction of the target and of -11.5 dB (0.0715) in the broadside direction, pointing toward each other. It also assumes a wavelength of 1.3 m and a back scatter coefficient σ of 1. These are the values corresponding to the strip dipole antennas described in Chapter 4, transmitting toward a reflective target with a radar cross section of 1 m^2 (0 dB). The thermal noise floor P_n is also estimated using the equation

$$P_n = kTB,$$
(5.28)

where k is Boltzmann's constant, T is the system temperature of 1000 K, and B is the bandwidth of 30 MHz.[23] This produces a thermal noise floor estimate of -124 dB relative to one watt, or -94 dBm relative to one milliwatt.

[23] Long *et al.*, *Microwave Radar and Radiometric Remote Sensing*, 2015.

Equation 5.26 and Equation 5.27 give the ratio of received power to transmitted power for bleedthrough and target return signals. These are the relationships represented in Figure 5.11. When a chirp is transmitted, received, and range-compressed, then the power in the bleedthrough and target range bins is dependent on the length of the chirp. Since
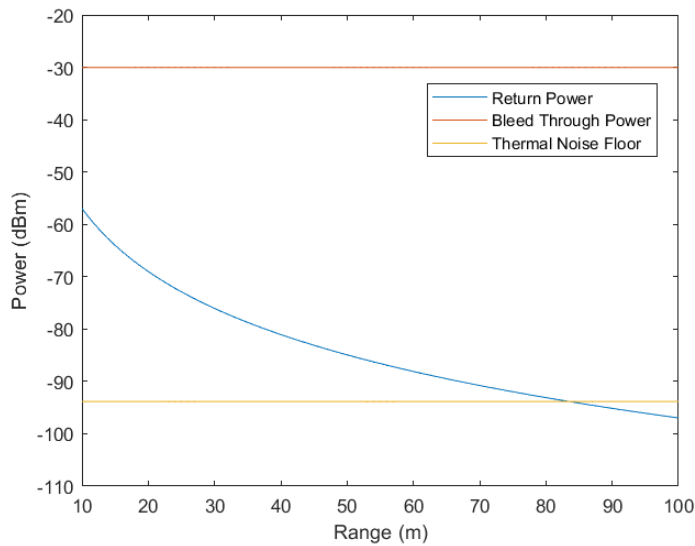
Figure 5.11: Power in the bleedthrough signal, the return signal, and the noise floor across various target ranges.

the DFT is a linear transform, the power in the bleedthrough and target range bins increases proportionally to N^2, where N is the number of samples in the chirp and the length of the DFT. Power in the other range bins (noise power) increases proportionally to N, so signal to noise ratio (SNR) increases proportionally to $N^2/N = N$. In other words, doubling the length of the chirp increases the SNR by 3 dB.

A reflective target with a radar cross section of 1 m² (0 dB) at a range of 10 m from the radar, the target return power is -27 dB relative to the bleedthrough power. This falls to -39 dB at 20 m, -46 dB at 30 m, -51 dB at 40 m, and -55 dB at 50 m ranges. Clearly, there will be issues attempting to measure weak return signals when such a dominant bleedthrough signal is present.

The bleedthrough signal can be reduced through a technique called feed-through nulling. Feed-through nulling consists of measuring or estimating the bleedthrough signal and subtracting that estimate from the received signal. Feed-through nulling can be applied in software or in hardware. Both methods are discussed below.

5.4.2 Digital Feed-through Nulling

Digital feed-through nulling is accomplished by subtracting samples of an estimate of the bleedthrough signal from samples of the received signal. There exist several methods for estimating the bleedthrough signal. One of the most effective methods creates an estimate by transmitting and receiving a chirp when there are no targets present. [1]

This type of feed-through nulling requires coherence between measurements, meaning that the SDR-antenna system must be stable enough to produce the same bleedthrough signal before and after targets are

[1] Kohls, "Software Defined Radio Short Range Radar," 2021.

added. This means that the antennas must not be moved relative to each other, and the LimeSDR Mini transmitter must not be turned off, or else the SDR may reinitialize with a different system impulse response. If there is coherence between the measurement to capture the bleedthrough signal and the measurements taken during radar operation, then the bleedthrough signal can be subtracted out from the received signal in the time domain.

Digital Feed-through Nulling Demonstration

Digital feed-through nulling can be demonstrated by simulating a radar-target system with a set of transmission line cables and a few other hardware components. The radar is set up by connecting a power divider to the transmitter to split the transmitted signal along two paths. One path is a 1 m cable with a 10 dB attenuator, representing the bleedthrough path, and the other is a 150 m cable, representing the 2-way path to a distant target. A power combiner is used to add the signals from both paths together, and the output of the power combiner is connected to the receiver. Figure 5.12 shows the layout of the test.
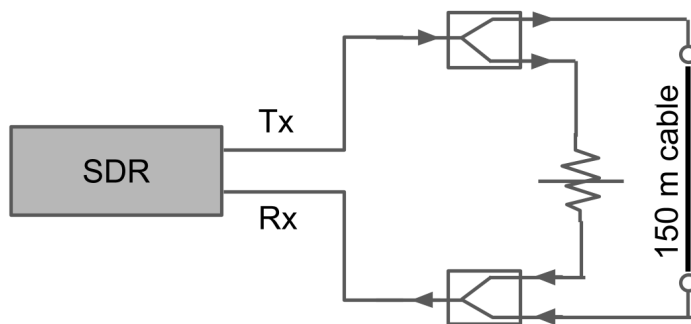

Figure 5.12: Hardware layout of the digital feed-through nulling test. A power divider splits the transmitted signal along two paths. One path is short with an attenuator, and one path is 150 m long with no attenuator.

The system now contains a short "bleedthrough" path and a long "target" path. The short path has a 10 dB attenuator to prevent the bleedthrough signal from decreasing the receiver sensitivity relative to the target signal.

First, the bleedthrough signal is collected. This requires removing the target path. The long cable is disconnected from the power combiner, and a 50-ohm resistor is used to terminate the cable and the power combiner input. The termination prevents reflections from altering the bleedthrough signal. A LFM chirp is transmitted and received by the SDR, and stored for later.

Next, the radar measurement is collected. This is the receive signal including the bleedthrough signal and the target return signal. To do this, the 50-ohm terminators are removed and the long cable is reconnected to the power combiner. An LFM chirp is again transmitted and received.

Finally, the samples from the bleedthrough measurement are subtracted elementwise from the samples of the radar measurement, producing the feed-through-nulled receive signal. Figure 5.13 shows the range-compressed data produced from the bleedthrough samples, and shows a high-power spike near the zero-range bin. Figure Figure 5.14 shows the range-compressed data from the received signal, with and without feed-through nulling. The result is that the bleedthrough signal is reduced by 22 dB, which lowers noise levels and improves the SNR at the 150 m target by 8 dB.
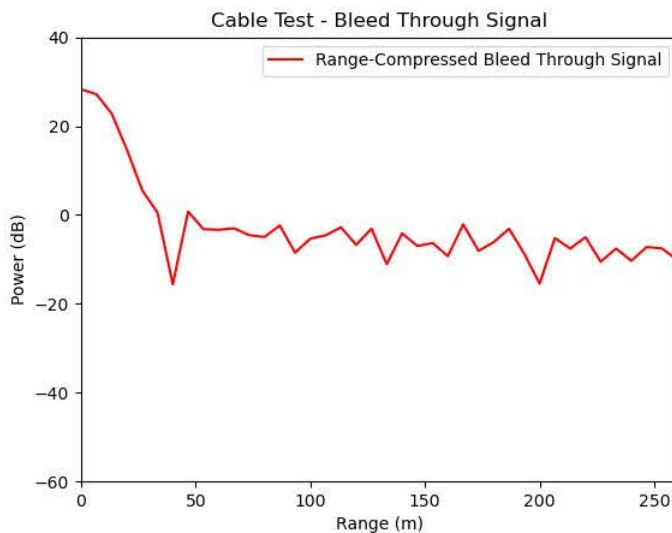

Figure 5.13: The range-compressed bleedthrough signal. The bleedthrough path is the only available path from the transmitter to the reciever, so power is concentrated in the 0 m range bin.

Here we can see that the bleedthrough signal is especially problematic for targets at close range. The bleedthrough sidelobes can overwhelm the return signal, making it difficult or impossible to detect.

One shortcoming of this experiment is that it does not represent the correct power levels for the bleedthrough signal and the return signal that would be encountered in an antenna transmission test. Another is that it requires many components and transmission line cable adapters and connections, which introduce spurious reflections. The test remains valuable, however, as a demonstration of the benefits of digital feed-through nulling.

5.4.3   Analog Feed-through Nulling

feed-through nulling can also be applied in RF hardware, rather than in software processing. This is done by dividing the signal that comes out of the SDR's transmit port. Some of the signal is sent to the antenna, and some is sent through RF components that perform a 180-degree phase shift on the signal, turning it into a feed-through null. A power
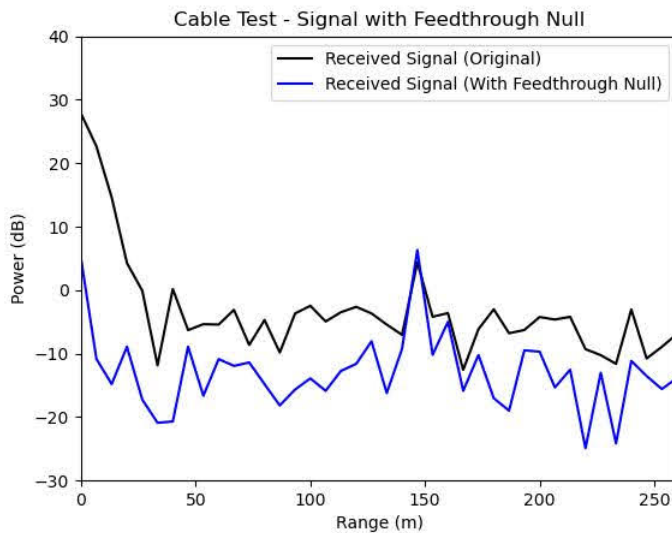
Figure 5.14: The range-compressed received signal with and without digital feedthough nulling. The target at 150 m is more easily visible when feed-through nulling is applied.

combiner is then used to add the feed-through null to the signal received by the antenna, eliminating the bleedthrough signal using destructive interference. When this is done effectively, it reduces the total power seen at the SDR receiver's frontend. This may improve receiver sensitivity, which is something digital feed-through nulling cannot do.

If you have access to the isolated digital bleedthrough signal, then applying digital feed-through nulling is much easier and simpler than applying analog feed-through nulling. To work, analog feed-through nulling requires matching the delay time, phase shift, and amplitude of the feed-through null to the physical bleedthrough signal. Any imprecision causes portions of the bleedthrough signal to leak into the received signal.

In a feed-through null, there are two ways to achieve a 180-degree phase shift. The optimal way is by using RF hardware which introduces a phase shift with no additional time delay. For example, this could be done by using a 180-degree hybrid coupler to divide the SDR's transmit signal into a signal for the antenna, and a lower-power signal with a phase change for the feed-through null. This method shown in Figure 5.15. For this method, the length L_1 of the feed-through transmission line is chosen such that the feed-through time delay is equal to the bleedthrough time delay.

The second way to achieve a 180-degree phase shift is by shortening or extending the feed-through null path by one half-wavelength relative to the bleedthrough path. This method shown in Figure 5.16. For this method, the length L_2 of the feed-through null transmission line is chosen so that the length of the feed-through null has a one-half wavelength difference from the length of the bleedthrough path. For a radar with
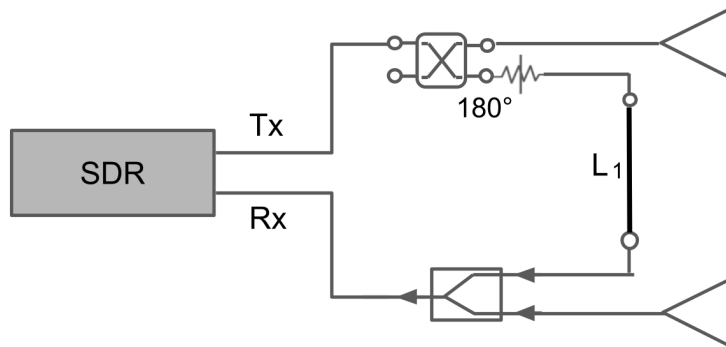
Figure 5.15: A system for analog feed-through nulling using a 180-degree hybrid coupler, an atteunuator, a transmission line of length L_1, and a power combiner.

a center frequency of 235 MHz, a half-wavelength is approximately 64 cm. Since the signal consists of a wideband chirp, this is only an approximation to the wavelength which changes throughout the course of the chirp, starting at 68 cm (220 MHz) and ending at 60 cm (250 MHz).
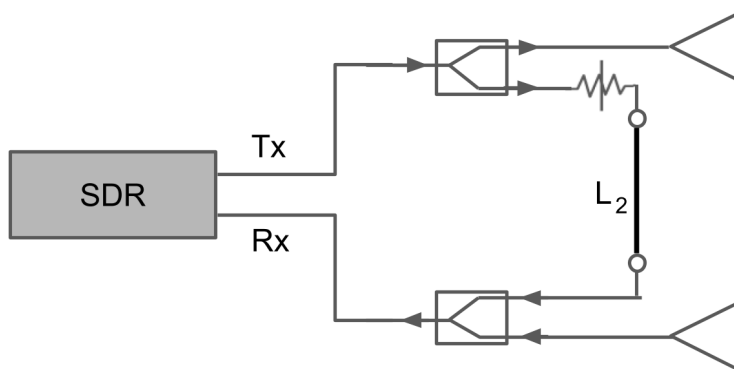
Figure 5.16: A system for analog feed-through nulling using a power divider, an attenuator, a transmission line of length L_2, and a power combiner.

The 4 centimeters offset at the beginning and end of the chirp means that the bleedthrough signal cannot be fully eliminated with this method. This type of analog feed-through null was simulated in MATLAB in order to understand the effects of the half-wavelength offset. Figure 5.17 shows the received signal before and after an analog feed-through null with a half-wavelength delay is applied. No targets are simulated.

At the center of the chirp, the bleedthrough signal is perfectly canceled by the feed-through null, but at the beginning and end of the chirp, some of the bleedthrough signal leaks through. This is because the
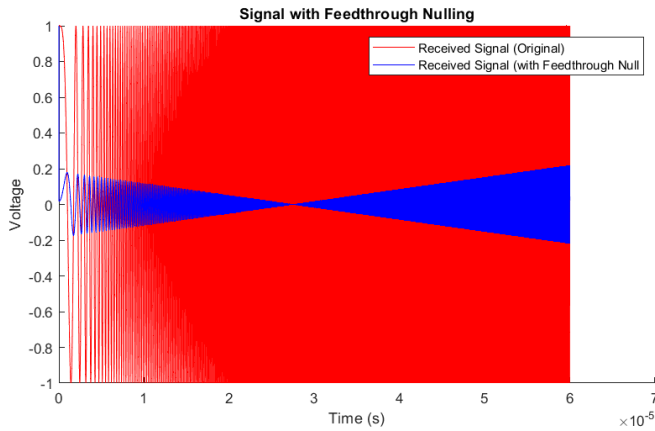
Figure 5.17: Simulation of a received signal with and without an analog feed-through null, where the phase change in the feed-through null is accomplished by delaying the feed-through null signal by one-half wavelength.

feed-through null does not have a 180-degree phase difference with the bleedthrough signal at these times. When both of the received signals are de-chirped and range-compressed, the result is counterintuitive. The simulated range-compressed data with and without the feed-through null is shown in Figure 5.18.
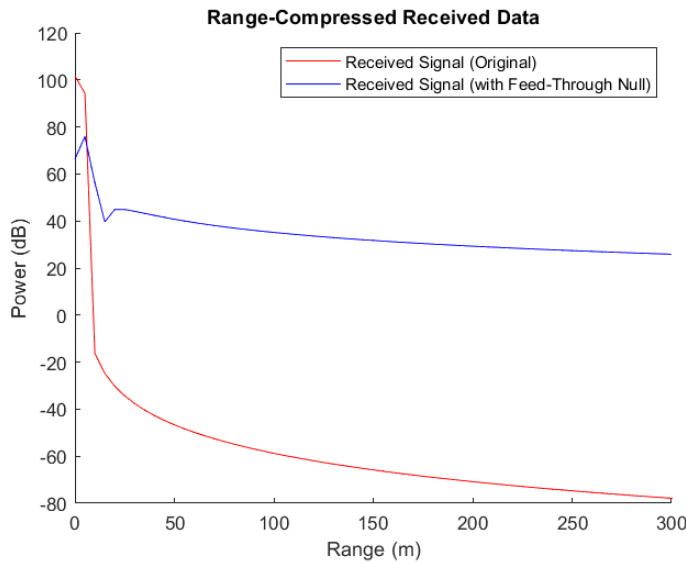
Figure 5.18: Range-compressed data with and without an analog feed-through null, where the 180-degree phase change is achieved with a half-wavelength delay. Although the feed-through reduces power in the bleedthrough 0 m range bin, it introduces high frequency content, which raises the noise across all other range bins.

The signal with feed-through nulling performs worse. Although the total power of the bleedthrough signal is reduced, the side lobes are high and extend over many range bins. They are so high that if there

were return targets, they would be easier to detect if there had been no feed-through null at all.

The reason for this has to do with the imperfect phase offset at the beginning and end of the signal. The original bleedthrough signal has the form of a LFM chirp. When this chirp is de-chirped, it becomes a tone, which corresponds to an impulse in the frequency domain. The partially-nulled bleedthrough signal shown in Figure 5.17 does not have the form of a chirp, and it becomes a very messy signal with high frequency content when it is de-chirped.

This effect can be countered if digital feed-through nulling is also applied, in addition to analog feed-through nulling. Since the analog feed-through null is coherent (the same every time the radio transmits a chirp), the reduced bleedthrough signal it produces can be measured and subtracted from subsequent received signals. As is typical for digital feed-through nulling, this requires a radar measurement when no targets are present. Figure 5.19 shows a simulation of the range-compressed data of a bleedthrough signal when a half-wavelength analog feed-through null is applied with and without a digital feed-through null. When the two feed-through nulling techniques are combined, the entire bleedthrough signal is removed. In real applications the bleedthrough signal may not be fully canceled, since that requires a system with perfect coherence. Nevertheless, it is important to include a digital feed-through if an analog feed-through system permits nontrivial bleedthrough leakage at either end of the transmitted chirp.
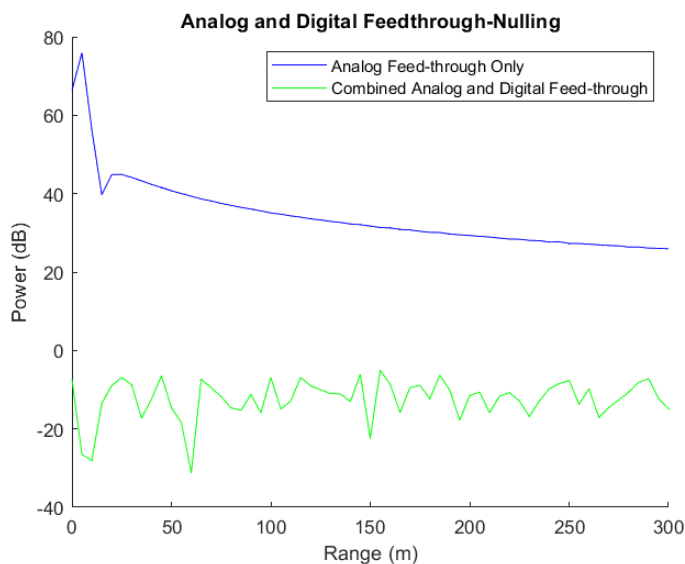

Figure 5.19: In simulations, the high-frequency content introduced by analog feed-through nulling can be removed by adding a digital feed-through null.

A much better way to construct an analog feed-through null is by keeping the travel time delay the same between the bleedthrough signal and the feed-through signal. This requires finding another way to

phase-shift the feed-through signal by 180 degrees. If done correctly, the feed-through null may be equally effective throughout the chirp. Under such a system, digital feed-through nulling is not required, but may still be beneficial. If there is a constant phase offset in the analog feed-through null, or if the amplitude of the feed-through null does not exactly match the amplitude of the bleedthrough signal, then digital feed-through nulling can catch and remove most of whatever bleedthrough signal is left.

Analog Feed-through Nulling Demonstration 1

As part of the radar development process, research was done into designing an analog feed-through null for the radar. To test the effectiveness of analog feed-through nulling, a simple test was designed in which a signal is split, a phase difference of 180 degrees introduced, and the signals recombined. Though simple, this test is considered useful because it indicates the bleedthrough cancellation loss achievable with the given components. If the signals cancel each other out at the combiner, then the same components might be used to perform feed-through nulling on the GPR.

The test is performed using layout in Figure 5.20. The phase shift is introduced with a 180-degree hybrid coupler, which divides the main signal into two signals with a 180-degree phase difference. The primary output of the hyprid coupler has higher amplitude than the coupled output, so attenuators are added to the signal paths until the amplitudes are matched. To prevent the high-frequency noise encountered in analog feed-through simulations, the paths of the primary signal (representing the bleedthrough signal) and the coupled signal (representing the feed-through signal) are made as close to the same length as possible, with an estimated accuracy of ±2 cm. With their amplitudes matched and their phase offsets equal to 180 degrees, measurements are collected. Data collected in this manner was used to produce Figure 5.21 and Figure 5.22.

The signals are acquired as follows. First, the bleedthrough signal is collected by disconnecting the transmission line cable in the feed-through path from the power combiner and terminating both ports with a matched load. Then, a chirp is transmitted and received. Next, the feed-through signal is collected by reattaching the feed-through transmission line cable to the power combiner, and by disconnecting the bleedthrough line from the power combiner, terminating each port. Finally, the combined received signal is collected by reattaching the bleedthrough transmission line, adhering to the setup shown in Figure 5.20, and by transmitting and receiving a radar chirp.

The result is a successful reduction of power at the receiver by 25 dB relative to the uncanceled bleedthrough signal. In addition, large side lobes in the range-compressed data are reduced to the noise floor. This demonstrates that analog feed-through nulling may be effective in reducing GPR bleedthrough signal and in improving receiver sensitivity.

Figure 5.20: A received signal is formed by adding the bleedthrough signal and the feed-through signal. The signals cancel each other out, resulting in a diminished received signal.

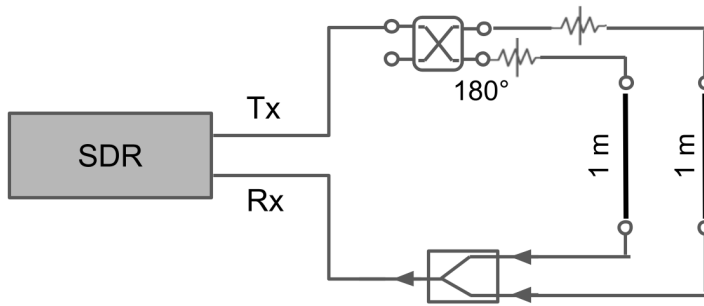

Figure 5.21: A received signal is formed by adding the bleedthrough signal and the feed-through signal. The signals cancel each other out, resulting in a diminished received signal.
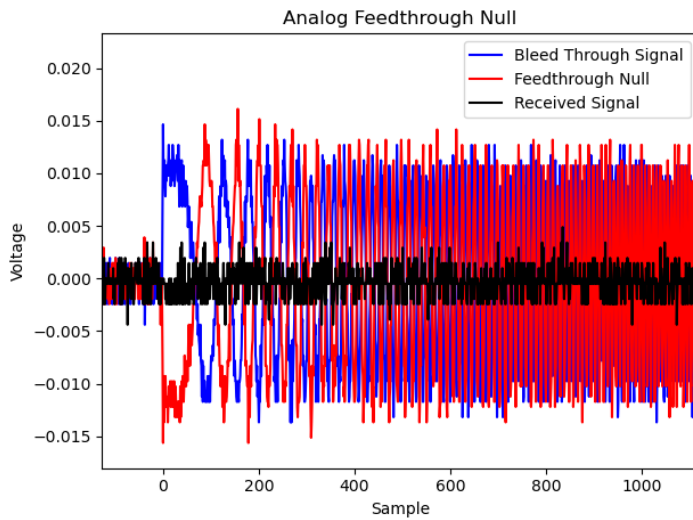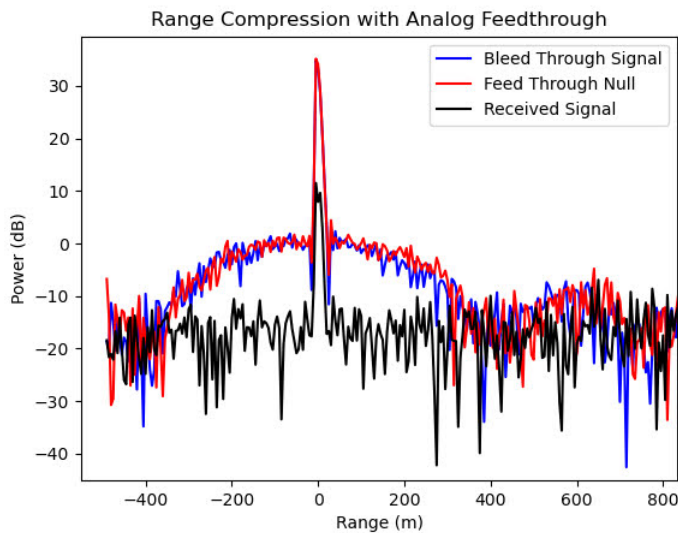
Figure 5.22: Range compression of a received signal formed by adding a bleedthrough signal and a feed-through signal. The bleedthrough and feed-through signals cancel out, resulting in lower received power in the 0 m range bin.

Analog Feed-through Nulling Demonstration 2

A follow-on experiment was designed to demonstrate that analog feed-through nulling may be used to reduce bleedthrough power in a cabled radar simulation. In the last test, there was only one path for the transmitted signal to take (excluding the feed-through path). A cable test similar to the one described in Section 5.4.2 provides two paths for a transmitted signal, one representing the bleedthrough path, and one representing a reflection off a target. In this system, the feed-through null ought to reduce the bleedthrough power, without reducing the target return signal.

This test was not successful. Difficulties in acquiring necessary components and in attempts to fine-tune the system prevented the author from eliminating the bleedthrough signal. Nonetheless, it is useful to discuss the experiment, as it highlights some of the difficulties and shortcoming associated with analog feed-through nulling.

The intended configured for the test is shown in Figure 5.23. This layout splits the signal twice, so that three paths are created, including the feed-through path, the bleedthrough path, and the target path. The length L_1 of the feed-through transmission line is selected such that L_1 is equal to L_2 plus any additional length on the bleedthrough path resulting from the connections to the power divider and power combiner. The feed-through and bleedthrough paths are short and equal, while the target path is 150 m long.

By the test's design, the attenuators in the feed-through path and the bleedthrough path cause the two signals to have the same amplitude, though the phases are opposite. As a result, when the signals are
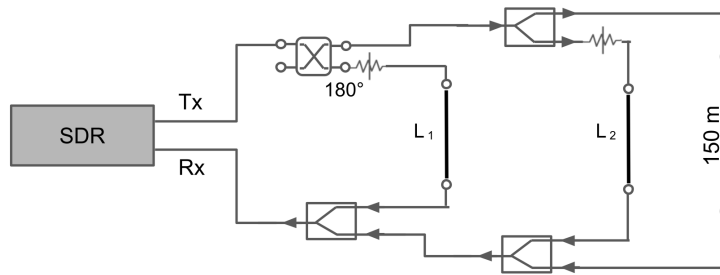
Figure 5.23: Configuration for a test to demonstrate analog feed-through nulling with a cable-radar test.

all combined before entering the receiver front end, the feed-through signal eliminates the bleedthrough signal. The expected result is that in the range-compressed data, bleedthrough power is reduced relative to the bleedthrough power that exists when the feed-through signal is disconnected. By reducing the bleedthrough power, one expects to improve the detectability of the target return signal.

When this experiment was attempted, it proved too difficult to simultaneously align the phases, the amplitudes, and the path lengths of the bleedthrough and feed-through signals. BNC cables and connectors were used, and the hardware available included cables at standard lengths and attenuators with standard attenuation levels (-3 dB, -6 dB, -10 dB, -20 dB). To complicate things, different attenuators caused different phase changes within the signal, some by as much as 20 degrees. As a result, adding components to improve amplitude matching resulted in difficult-to-predict changes in the phase matching, and changed the length of the travel path. In fact, attempts to match any one variable likewise resulted in changes to all the other variables.

The design process for a feed-through system is much easier if one has access to variable attenuators and variable phase shifters. Another useful tool could be transmission lines of variable length which preserve their characteristic impedance across different lengths[24].

Figure 5.24 shows the mostly-unmatched bleedthrough and feed-through signals from one configuration of the cable radar test. Though they are off in phase and amplitude, they add to form the received signal which has 2 dB lower power than the bleedthrough signal alone. This is evidenced in the lower amplitude of the de-chirped signal in Figure 5.25 and in the lower power in the range-compressed data displayed in Figure 5.26.

Results could be dramatically improved by using variable attenuators and variable phase-shifters to tune the feed-through signal to the bleedthrough signal. However, this would require expensive components often costing hundreds of dollars each, which undermines the project goal of producing a low-cost Software-Defined Radio GPR. Another challenge is that implementing analog feed-through nulling on the GPR

[24] McAlister, "A variable-length radio-frequency transmission-line section," 1951.
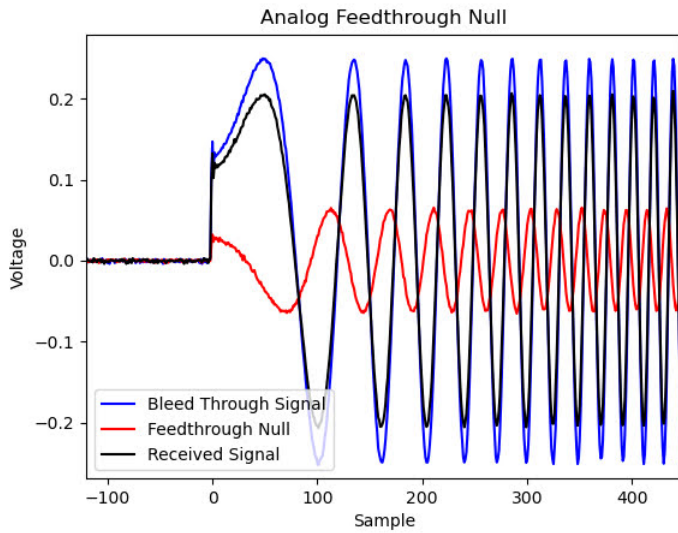
Figure 5.24: Received bleedthrough and feed-through signals, though not perfectly matched in phase and amplitude, partially cancel to produce the combined received signal.
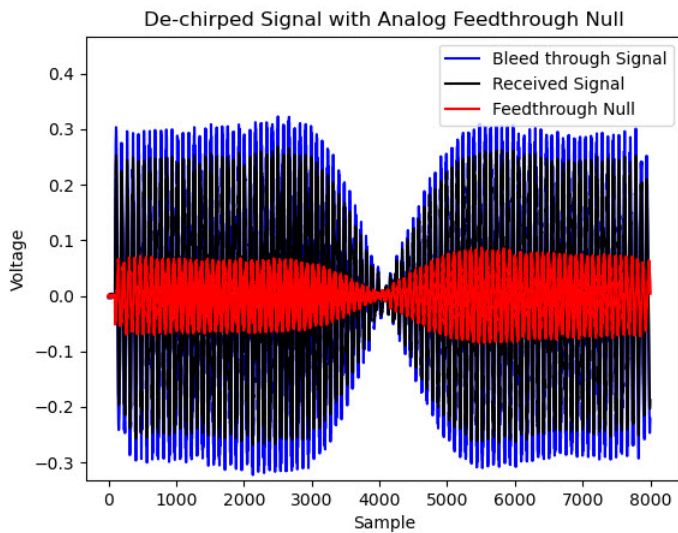

Figure 5.25: De-chirped data for a bleedthrough and a feed-through signal. When added, they partially cancel out, creating the received signal
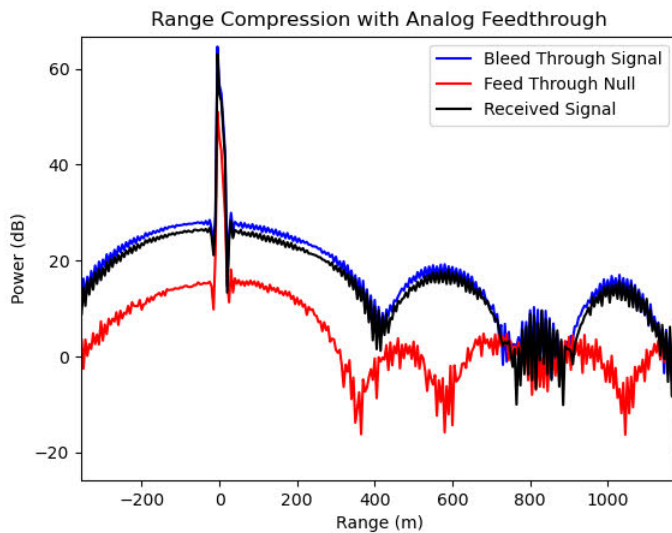
Figure 5.26: Range-compressed data for a bleedthrough signal and a feed-through signal. The received signal is the time-domain sum of the bleedthrough and feed-through signals. The feed-through signal partially cancels out the bleedthrough signal, resulting in a received signal which has lower power in the bleedthrough range bins.

would add considerable weight to the drone GPR system, including (at a minimum) the weights of a hybrid coupler, a power combiner, and any necessary attenuators.

There are strengths to analog feed-through nulling as a method for bleedthrough power reduction. It lowers the power level at the SDR frontend, which can increase receiver sensitivity. It does not require a previous measurement in the absence of targets, unlike digital feed-through nulling. If such a measurement is available, then it can easily be combined with digital feed-through nulling for maximum effect.

The shortcomings of analog feed-through nulling are that it requires more components, which can be heavy and costly. It can be difficult to tune. In addition, it requires splitting the power emanating from the transmitter, which reduces the power transmitted by the antenna. If an analog feed-through system is designed for the GPR, these are likely to be the greatest design challenges that must be overcome.

5.5 Radar and Antenna Testing

The author performed a series of outdoor tests with the LimeSDR Mini radar using the strip dipole antennas. The goal of the tests was to measure the distance to a corner reflector at various distances between 5 and 30 m away from the radar.

5.5.1 Outdoor Radar Testing

The feed-through nulling techniques discussed in this thesis were applied in radar tests with the goal of comparing their relative effectiveness. The

most effective technique for bleedthrough reduction was the digital feed-through null. Without digital feed-through nulling, a typical range-compressed radar measurement contained a bleedthrough signal 47 dB above the noise floor. Spectral leakage from the bleedthrough signal extended anywhere from 8 to 20 dB above the noise floor in the 5 m to 30 m range bins, depending on the range and on variables such as window selection. The digital feed-through null reduced the bleedthrough power by 26 dB. Unfortunately, despite this bleedthrough reduction, the target remained invisible below the noise floor for many tests. Efforts to improve sensitivity by averaging measurements together were met with limited success.

A review of the initial tests revealed that the high noise floor was likely a result of the test location that was selected. The radar was tested on the campus of Brigham Young University, in a field with approximate size 60 m x 60 m. There were several trees which blew in the wind and vehicles which drove on the adjacent roads, all of which likely contributed to higher noise in the corresponding range bins.

The same corner reflector was successfully detected in a later test conducted by fellow Brigham Young University student Gideon (Levi) Powell. This was accomplished by testing the LimeSDR Mini radar on the roof of a campus building rather than in a field. This location was more suitable for radar testing as it was out of the line of sight of moving objects like trees, vehicles, and students. In this test, the radar transmitted and captured 300 chirps, with one additional chirp that was used as a reference bleedthrough signal for feed-through nulling. The first 50 measurements were captured without any target present. Around measurement 51, a corner reflector was positioned directly in front of the antennas and slowly moved back. The corner reflector has an effective area A_e of 0.74 m^2 and a radar cross section of $\sigma = 2$ (3 dB), where the radar cross section[25] is given by

25 Rulf, "The effective area of a corner reflector," 1991.

$$\sigma = 4\pi \frac{A_e^2}{\lambda^2}. \tag{5.29}$$

The de-chirped data and range-compressed data generated from the radar measurements are shown in Figure 5.27. The data was produced using digital feed-through nulling.

In the dechirped data, undulations in signal amplitude can be seen spanning samples 50 to samples 150. These are caused by phase shifts in the signal reflecting off the corner reflector, which interfere constructively and destructively with reflections off other surfaces like the roof on which the test took place. In the range-compressed data, a blue arrow shows the path of the corner reflector throughout the measurements. The range bins show an increase in power when the corner reflector passes through them. This increase in power is especially noticeable when compared to the unchanged power in the first 50 measurements.

A similar follow-up test was conducted by the author in an empty parking lot, producing the results shown in Figure 5.28. In this test, 160
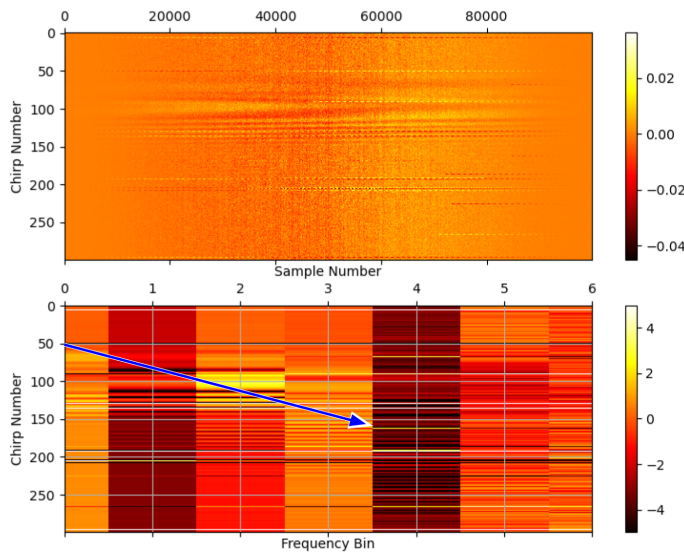
Figure 5.27: Data collected on the LimeSDR Mini radar. Of the 300 measurements collected, the first 50 had no target. Measurements 51-300 were taken as a corner reflector was moved slowly away from the radar to a max range of approximately 15 m. The top plot displays the de-chirped data. The bottom plot displays the range-compressed data for the bleedthrough signal and the 6 adjacent range bins. The blue arrow indicates the approximate path of the corner reflector.

measurements were collected as a corner reflector was moved continuously from a distance of 20 m up to 5 m away from the radar. The target was kept at ground level to prevent the multipath effect encountered in the previous test. The measurements preceding the zero measurement on the y axis are measurements of the bleedthrough signal (collected before the target was placed in the system) and are included to illustrate the difference in received power before and after the feed-through null is applied.

In this test, the target is expected to be seen in the 20 m range bin from approximately measurements 0 to 50, the 15 m range bin from measurements 51 to 100, the 10 m range bin from measurements 101 to 150, and the 5 m range bin from measurements 150 to 160. It is also expected that the power fluctuate in adjacent bins as the target passes between range bin centers. Range bins 5, 10, and 20 show increased power where expected, although range bin 15 fails to display power far above the noise floor at any point in the test. Additionally, there are strong sidelobes, evidenced in multiple vertical lines such as those spanning measurements 0 to 50. The cause of these sidelobes is unclear and requires further investigation. Despite these peculiarities, there is a general trend in power that begins at the 20 m range bin and moves down to the 5 m range bin over the course of the measurements, following the route of the target. The radar's maximum SNR occurs during the final ten measurements, where the power in the 5 m range bin is roughly
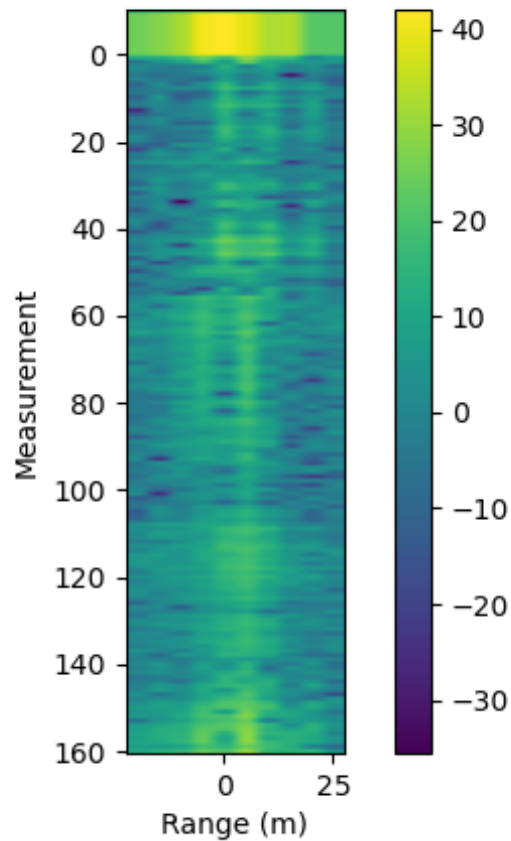
Figure 5.28: Range compressed data produced by the radar when a corner reflector with radar cross section of 3 dB was positioned 20 meters away from the radar at measurement 0, then moved up continuously until it was 5 meters away at measurement 150. The bleedthrough signal is displayed in measurements preceding and including the 0 measurement.

22 dB higher than the noise floor.

5.5.2 Calculated vs Observed SNR

It is useful to compare the expected SNR of the radar with the observed SNR. The highest SNR achieved in the last radar test is approximately 22 dB, which is achieved in the 5-meter range bin during the final measurements shown in Figure 5.28. Sidelobes cause high power to appear in the adjacent range bins but fall off in more distant bins.

In Section 5.4.1, the expected power in the bleedthrough signal, the return signal, and noise floor were simulated for various target ranges using Equation 5.26, Equation 5.27, and Equation 5.28 and were plotted in Figure 5.11. These equations yield a predicted return power from the corner reflector at a 5-meter range of at least -50 dBm, compared to the theoretical thermal noise floor of -94 dBm. That means the radar has the theoretical potential for an SNR of 44 dB, whereas testing demonstrated

an SNR of 22 dB in the best-case scenario. There is a discrepancy of 22 dB.

Discrepancies between the theoretical best-case SNR and achieved SNR are common because in practice, the noise floor is rarely dominated by the thermal noise floor. Interference arises from many sources including competing in-band signals and high-power out-of-band signals which are not sufficiently removed with filtering. Another source of interference includes the bleedthrough signal, which is analytically calculated to be 64 dB above the thermal noise floor. Although this is mostly removed using digital feed-through nulling, the full bleedthrough power is experienced at the SDR receiver frontend and can further limit the sensitivity of the receiver. Imperfections in RF components such as the antennas and cables increase the system noise figure, further reducing the SNR.

For the radar SNR to be increased, some of these interference sources must be reduced, or the return power must be increased. Some ways that this might be achieved are by testing with larger targets, testing in remote locations, or by using higher-gain antennas. Performance would also improve if the radar used increased bandwidth, which would decrease the noise power in individual range bins while improving the range resolution. Increasing the bandwidth is not possible with the current SDR, which only supports a 30 MHz bandwidth due to its 30 MHz IQ sampling rate.

A key thing to recognize is that the target can be difficult to identify on its own, but it is easier to recognize patterns that change through time. This is a key concept for many GPR systems. As a GPR moves over the surface of the ground, as long as the GPR measurements hold steady the operator may assume that the layers of underground medium are relatively consistent. A relative change in GPR readings indicates that something new has been encountered, whether that's a rock, a pocket of water, or a fissure below the surface.

When the LimeSDR Mini radar is eventually employed for glacial drone GPR applications, it is expected that it will highlight the relative changes in glacial layers across different regions of the glacier. While the outdoor tests have employed a target with a radar cross section of 3 dB, the GPR will measure large sheets of snow and ice with much higher radar cross sections, increasing the return power and the SNR of the received signal.

Conclusion

6

6.1 Conclusion

The LimeSDR Mini can perform short-range LFM radar. It is probably possible to use the LimeSDR Mini to construct a reasonably effective drone GPR if it used in a low-noise and low-interference environment. The strengths of the LimeSDR Mini are that it is affordable and lightweight. Its shortcomings include a lack of support for TX-RX synchronization and its low sampling rate, which only supports a radar range resolution of 5 m. The synchronization issue can be solved by measuring the system impulse response of the SDR at initialization and applying deconvolutional correction.

It is shown that the radar can identify targets if it is in an environment without dynamically moving objects such as humans and vehicles. To successfully pick out moving targets, measurements must be coherent, meaning that the only significant changes between consecutive measurements arise from changes in the targets of interest. Although this is difficult to achieve in an urban environment, it is easier in remote areas including glaciers. Even in the static, unmoving conditions of a glacier, the radar must employ methods for bleedthrough signal reduction. Of the methods explored in this thesis, digital feed-through nulling is the most effective. Digital feed-through nulling can be accomplished by taking a measurement in the absence of targets (for example, by flying the drone at least 50 m above the surface of the Earth), and subtracting that measurement from subsequent measurements of the ground.

6.2 Future Work

The possibility for the LimeSDR Mini as a drone GPR comes down to whether or not the radar is sensitive enough to perceive changes in subterranean material at various depths. For this reason, the next steps in GPR development must include radar testing in GPR applications. The radar must be tested in a static environment distant from vehicles and human foot traffic, preferably in a location with known variations in subterranean material. Snowy terrain is desirable in order to resemble glacier environments, although success in sandy or otherwise dry ground may also correspond to good performance in snow and ice. Radar measurements can be taken as the GPR is moved across the ground by a sled or trailer. If radar measurements in these scenarios are too noisy to

be reliably interpreted, then the LimeSDR Mini is unlikely to succeed as the standalone radio system for drone GPR.

If it can be verified that the LimeSDR Mini radar can identify material changes at various depths underground, then the next step in development will be to construct a fully-contained standalone radar system which can be mounted to the drone. The complete radar system must include the LimeSDR Mini, the transmitting and receiving antennas and their associated connectors, a supporting Raspberry Pi, and a power supply consisting of rechargeable batteries. Once the portable system is constructed, assuming it is within the 5 lb weight requirement, it will be ready for drone-GPR field testing, whether on glaciers or elsewhere.

References

1   Kohls, N. E., "Software Defined Radio Short Range Radar," Master's thesis, Brigham Young University, 2021.   *cited on pp. 2, 15, 34*

2   Elsevier Publishing Co, *The Nobel Prize in Physics 1909- Guglielmo Marconi Biographical*, 1967. URL: https://www.nobelprize.org/prizes/physics/1909/marconi/biographical/.   *cited on p. 4*

3   Hülsmeyer, C., *Christian Hülsmeyer and the Early Days of Radar, a Survey. Part II*, 1904. URL: https://www.cdvandt.org/Huelsmeyer%5C%20part%5C%20II.pdf.   *cited on p. 4*

4   Watson Jr, R. C., *Radar Origins Worldwide: History of its evolution in 13 nations through World War II*. Trafford Publishing, 2009.   *cited on pp. 4, 5*

5   Blindow, N., Eisenburger, D., Illich, B., Petzold, H., and Richter, T., "Ground penetrating radar," *Environmental Geology: Handbook of Field Methods and Case Studies*. Berlin, Heidelberg: Springer Berlin Heidelberg, 2007, pp. 283–335. DOI: 10.1007/978-3-540-74671-3_10   *cited on p. 4*

6   SPH Engineering, *Webinar: Basics of ground penetrating radar (GPR) usage with a drone*, 2023. URL: https://www.sphengineering.com/news/webinar-basics-of-ground-penetrating-radar-gpr-usage-with-a-drone.   *cited on p. 5*

7   MALÅ, *Airborne Ground Penetrating Radar System: GeoDrone - Airborne GPR made easy*, 2021. URL: https://www.malagpr.com.au/geo_gpr_drone.html.   *cited on p. 5*

8   UgCS - SPH Engineering, *Expedition to Locate P-38 "Echo" From Lost Squadron just Returned from Greenland's Ice Cap*, June 2023. URL: https://www.ugcs.com/news-entry/expedition-to-locate-p-38-echo-from-lost-squadron-just-returned-from-greenland-s-ice-cap.   *cited on p. 5*

9   Jensen, K., *Glacier Girl: The back story - How it got trapped in the ice, and how it got out*, July 2007. URL: https://www.smithsonianmag.com/air-space-magazine/glacier-girl-the-back-story-19218360/.   *cited on p. 5*

10 Easton Jr, R. L., *Fourier Methods in Imaging*. John Wiley & Sons, 2010.

11 BniLam, N., Joosens, D., Steckel, J., and Weyn, M., "Low Cost AoA Unit for IoT Applications," *2019 13th European Conference on Antennas and Propagation (EuCAP)*, 2019, pp. 1–5.   *cited on p. 11*
                    cited on p. 11

12 White, K., *Science & Engineering Indicators*, December 2019. URL: https://ncses.nsf.gov/pubs/nsb20206/publication-output-by-region-country-or-economy.   *cited on p. 13*

13 Prabaswara, A., Munir, A., and Suksmono, A. B., "GNU Radio based software-defined FMCW radar for weather surveillance application," *2011 6th International Conference on Telecommunication Systems, Services, and Applications (TSSA)*, IEEE, 2011, pp. 227–230.

cited on p. 13

14 Jędrzejewski, K., Malanowski, M., Kulpa, K., Krysik, P., and Pożoga, M., "Passive Space Object Observation using LOFAR Radio Telescope and Software-defined Radio Receiver," *2022 19th European Radar Conference (EuRAD)*, 2022, pp. 1–4. DOI: `10.23919/EuRAD54643.2022.9924994`

cited on p. 13

15 Hristov, S., Daniel, L., and Gashinova, M., "Software defined radio for profile reconstruction in forward scatter radar," *2014 11th European Radar Conference*, 2014, pp. 573–576. DOI: `10.1109/EuRAD.2014.6991335`

cited on p. 13

16 Carey, S. C. and Scott, W. R., "Software defined radio for stepped-frequency, ground-penetrating radar," *2017 IEEE International Geoscience and Remote Sensing Symposium (IGARSS)*, 2017, pp. 4825–4828. DOI: `10.1109/IGARSS.2017.8128082`

cited on p. 13

17 Lime Microsystems Ltd., *LimeSDR Mini*, 2020. URL: `https://limemicro.com/products/boards/limesdr-mini/`.

cited on p. 14

18 British Amateur Television Club, *LimeSDR Mini Output Power Levels*, January 2019. URL: `https://wiki.batc.org.uk/LimeSDR_Mini_Output_Power_Levels`.

cited on p. 14

19 DJI, *Matrice 600 pro user manual*, English, version 1.0, DJI, 2017.

cited on p. 17

20 Livingston, T. A., "Comparison of Compact Very High Frequency (VHF) Antennas for Small Airborne Ground Penetrating Radar," Master's thesis, Brigham Young University, 2023, not yet published.

cited on p. 20

21 Harris, F. J., "On the use of windows for harmonic analysis with the discrete Fourier transform," *Proceedings of the IEEE*, Vol. 66, No. 1, 1978, pp. 51–83.

cited on p. 24

22 LDS Dactron, *Application Note AN014 - Understanding FFT Windows*, 2003. URL: `https://www.egr.msu.edu/classes/me451/me451_labs/Fall_2013/Understanding_FFT_Windows.pdf`.

cited on p. 24

23 Long, D. and Ulaby, F., *Microwave Radar and Radiometric Remote Sensing*. Artech, 2015.

cited on p. 33

24 McAlister, K., "A variable-length radio-frequency transmission-line section," *Journal of Scientific Instruments*, Vol. 28, No. 5, 1951, p. 142.

cited on p. 44

25 Rulf, B., "The effective area of a corner reflector," *IEEE Antennas and Propagation Magazine*, Vol. 33, No. 2, 1991, pp. 48–. DOI: `10.1109/74.88189`

cited on p. 47